AMERICAN
METEOROLOGICAL
SOCIETY

Journal of Climate

The DOI for this manuscript is doi: 10.1175/2010JCLI3389.1

Seasonal variability of the Atlantic meridional overturning circulation at 26.5°N

Date: 26.05.2010

T. Kanzow[1,2], S.A. Cunningham[2], W.E. Johns[3], J. J-M. Hirschi[2], J. Marotzke[4], M. O. Baringer[5], C.S. Meinen[5], M. P. Chidichimo[4], C. Atkinson[2], L. M. Beal[3], H. L. Bryden[2], J. Collins[6]

Corresponding author: T. Kanzow (tkanzow@ifm-geomar.de, +49 431 6004150)

[1]Ozeanzirkulation und Klimadynamik, Leibniz-Institut für Meereswissenschaften an der Universität Kiel, Düsternbrooker Weg 20, 24105 Kiel, Germany

[2]Ocean Observation and Climate Group, National Oceanography Centre, Empress Dock, Southampton, SO17 3ZH, U.K.

[3]Division of Meteorology and Physical Oceanography, Rosenstiel School of Marine and Atmospheric Science, 4600 Rickenbacker Causeway, Miami, FL 33149-1098, U.S.A.

[4]Ozean im Erdsystem, Max-Planck-Institut für Meteorologie, Bundesstraße 53, 20146 Hamburg, Germany

[5]Physical Oceanography Division, NOAA Atlantic Oceanographic and Meteorological Laboratory, 4301 Rickenbacker Causeway,Miami, FL 33149, U.S.A.

[6]British Oceanographic Data Centre, 6 Brownlow Street, Liverpool, L3 5DA, United Kingdom

Abstract

The Atlantic meridional overturning circulation (AMOC) makes the strongest oceanic contribution to the meridional redistribution of heat. Here, an observation-based, forty-eight-month-long time series of the vertical structure and strength of the AMOC at 26.5°N is presented. From April 2004 to April 2008 the AMOC had a mean strength of 18.7 ±2.1 Sv with fluctuations of 4.8 Sv rms. The best guess of the peak-to-peak amplitude of the AMOC seasonal cycle is 6.7 Sv, with a maximum strength in autumn and a minimum in spring. While seasonality in the AMOC was commonly thought to be dominated by the northward Ekman transport, this study reveals that fluctuations of the geostrophic mid-ocean and Gulf Stream transports of 2.2 Sv and 1.7 Sv rms, respectively, are substantially larger than those of the Ekman component (1.2 Sv rms). A simple model based on linear dynamics suggests that the seasonal cycle is dominated by wind stress curl forcing at the eastern boundary of the Atlantic. Seasonal geostrophic AMOC anomalies might represent an important and previously underestimated component of meridional transport and storage of heat in the subtropical North Atlantic. There is evidence that the seasonal cycle observed here is representative of much longer intervals. Previously, hydrographic snapshot estimates between 1957 and 2004 had suggested a long-term decline of the AMOC by 8 Sv. This study suggests that aliasing of seasonal AMOC anomalies might have accounted for a large part of the inferred slowdown.

1. Introduction

The Atlantic meridional overturning circulation (AMOC) plays a major role in the heat budget of the North Atlantic region. Hall and Bryden (1982) showed from observations that at 26°N the Atlantic circulation carries 1.3 ±0.3 PW of heat northward, mostly within the AMOC. Their results were subsequently confirmed by global ocean inverse analyses (e.g. Ganachaud and Wunsch, 2003). The heat carried by the AMOC accounts for one quarter of the maximum global meridional heat transport required by the coupled ocean-atmosphere system to balance the global radiation budget. The Intergovernmental Panel on Climate Change considers it "very likely" that the AMOC will significantly weaken over the 21st century as a consequence of anthropogenic greenhouse gas emissions (IPCC, 2007) thus reducing the oceanic supply of heat to the North Atlantic region. Model simulations also suggest natural AMOC variability on intraseasonal to multi-decadal timescales (e.g. Delworth et al., 1993; Jayne and Marotzke, 2001; Latif et al., 2004; Biastoch et al., 2008, Wunsch and Heimbach, 2009). A pronounced seasonal variability between the equator and mid-latitudes reflects seasonally varying Ekman transports (e.g. Jayne and Marotzke, 2001; Wunsch and Heimbach, 2009). Multi-decadal AMOC variability is thought to be linked to North Atlantic sea surface temperature changes (e.g., Delworth et al., 1993; Latif et al., 2004). However, owing to a lack of observations, the existence of this link in the real ocean remains uncertain (Kanzow and Visbeck, 2009).

The AMOC can be visualised as the meridional overturning streamfunction $\Psi(y,z,t)$ at any given latitude y by

$$\Psi(y,z,t) = \int_{z}^{0} \int_{x_W}^{x_E} v(x,y,z,t)\, \mathrm{d}x\, \mathrm{d}z \qquad (1),$$

where $v(x,y,z,t)$ is the northward velocity with x, z and t denoting the zonal, vertical and

time dimensions, respectively. The integration limits x_W and x_E stand for the zonal positions of the western and eastern boundaries of the Atlantic. Zonal hydrographic sections between 32°S and 56°N in the Atlantic suggest that Ψ consists of two (an upper and a lower) interhemispheric overturning cells (e.g. Talley et al., 2003; Fig. 1). The upper cell is characterized by a northward flow that reaches down to 1300 m and a southward return flow of North Atlantic Deep Water (NADW) between 1300 m and 4000 m. The overturning rate of the upper cell is estimated at 13 – 19 Sv (Fig. 1, Ganachaud and Wunsch, 2003; Lumpkin, 2007). The lower cell (Orsi et al., 2002) consists of northward flow of Antarctic Bottom Water (AABW) in the lower limb roughly below 5000 m (Fig. 1), with the transport diminishing northward due to entrainment of AABW into the overlying NADW, thereby requiring compensating southward NADW transport between 4000 and 5000 m (upper limb). At 26.5°N in the Atlantic the strength of the AABW cell amounts to 2 ±0.5 Sv (Bryden et al., 2005a).

Daily estimates of the basin-wide full-water-column integrated AMOC became available when the RAPID-MOC / MOCHA monitoring array (Kanzow et al., 2008a, Fig. 2) across the Atlantic along 26.5°N became operational in April 2004. During the first year of array observations the AMOC had a mean strength of the upper cell of 18.7 Sv, and an intra-seasonal variability of 5.6 Sv rms (Cunningham et al., 2007).

In this study we describe seasonal AMOC transport variations as observed by the RAPID-MOC / MOCHA array at 26.5°N between April 2004 and April 2008. First we present the data set and the methodology underlying the computation of the strength and structure of the AMOC (section 2). We then discuss the temporal variability and vertical structure of the AMOC, with a focus on seasonal anomalies (section 3). In section 4 a forcing mechanism

is proposed that accounts for a large fraction of the seasonal AMOC anomalies. Possible implications of our results are discussed in section 5. Conclusions are given in section 6.

2. Data and methods

a. Data

The three components of $\Psi(z)$ at 26.5°N are the Gulf Stream (T_{GS}), Ekman (T_{EK}) and mid-ocean (T_{MO}) transports (Kanzow et al., 2007; Cunningham et al., 2007). The bulk of northward Gulf Stream volume transport, T_{GS}, has been monitored using a submarine cable and repeated ship sections nearly continuously since 1982 (Larsen, 1992; Meinen et al., 2010). The vertical structure of $T_{GS}(z)$ is inferred from T_{GS} as described by Baringer et al. (2008).

The northward Ekman transport zonally integrated between the shelf of Abaco (Bahamas) and the African coast is estimated as the zonal integral of the zonal component of the wind stress from space borne Quickscat scatterometer measurements (Freilich and Dunbar, 1999; Schlax et al., 2001). T_{EK} is then assumed to be distributed evenly between the surface and 100 m, to obtain a vertical profile of transport per-unit depth $T_{EK}(z)$.

For the mid-ocean geostrophic transport T_{MO}, we use the RAPID-MOC / MOCHA moorings. To directly measure strong flows at the western boundary, moorings WB0, WB1, WB2 and WB3 (Fig. 3) are equipped with current meters at discrete levels distributed throughout the water column, and at WBA and WB0 the velocity field in the upper 500 m is profiled by upward-looking ADCPs (Johns et al., 2008). All records are 40 hour low-pass filtered, sub-sampled on a 12 hourly grid, and are subsequently interpolated onto a spatial grid of 0.5 km zonal and 20 m vertical resolution. Subsequently, profiles of

zonally integrated transport (per-unit-depth) over the 16 km wide western boundary wedge, $T_{WBW}(z)$, between the Abaco shelf and WB2 (Fig. 3) are computed (Johns et al., 2008).

The remainder of the mid-ocean is measured by moorings near the western and eastern boundaries of the Atlantic and on both flanks of the Mid-Atlantic Ridge, which record temperature (T) and salinity (S) at discrete depths (Fig. 2a,b). These records are calibrated , and subsequently 2 day low-pass filtered and sub-sampled at 12 hourly resolution (Kanzow et al., 2006; Kanzow et al., 2007). At the eastern boundary T and S data from several moorings have been merged into one profile from 4840 m to the shallowest available level during each deployment (Kanzow et al., 2007; Kanzow et al., 2009). The western boundary end-of-section profile uses data merged from WB2 shallower than 4000 m and from WBH1 / WBH2 (or WB3 after April 2005) at depths greater than that (Fig. 2b). At the western flank of the MAR mooring MAR1 provides T and S from the sea surface to 5000m and on the eastern flank MAR2 covers the 2500 – 5000 m interval (Fig. 2b). Filtered and sub-sampled T and S data at each site are vertically interpolated onto a 20 dbar grid (Kanzow et al., 2007), from which densities ρ are then computed. Vertical profiles of density at the western and eastern boundaries (ρ_W, ρ_E), and on the western and eastern flanks of the Mid-Atlantic Ridge (ρ_{MARW}, ρ_{MARE}) are used to compute zonally basin-wide integrated northward geostrophic transport per-unit-depth $T_{INT}(z)$ relative to a deep reference level z_{REF} = - 4740 m (Appendix A). Northward transports of Antarctic Bottom Water (AABW) at depths greater than 5000 m are accounted for by extending the transport profile to 6000 m using historical estimates (Appendix A). $T_{INT}(z)$ and $T_{WBW}(z)$ are used to compute the mid-ocean geostrophic transport (section 2b).

b. Methodology

Since each variable in this study is a function of *t*, the explicit mentioning of the time-dependence will be dropped hereafter. Throughout this study then $T_{GS}(z)$, $T_{EK}(z)$, $T_{MO}(z)$, etc. indicate profiles of transport per-unit-depth (Sv m^{-1}), whereas T_{GS}, T_{EK}, T_{MO}, etc., represent transports (Sv) integrated over a vertical range.

At each time step the strength of the AMOC, Ψ^{MAX}, will be defined as the maximum of the overturning stream function $\Psi(z,t)$ (or maximum northward upper-ocean transport), according to

[2] $$\Psi^{MAX} = \int_{-h_{ZC}}^{0} T_{AMOC}(z)dz ,$$

where $h_{ZC}(t)$ represents the depth of the lower boundary of the upper ocean northward flowing branch of the AMOC (Fig. 1) and T_{AMOC}(z) is the vertical profile of zonally integrated northward transport per-unit-depth - *i.e.* the sum of components $T_{EK}(z)$, $T_{GS}(z)$, and $T_{MO}(z)$ (Kanzow et al., 2009). Hence, before we can calculate Ψ^{MAX} we need to estimate $T_{MO}(z)$, which consists of two components, (i) $T_{WBW}(z)$, and (ii) the *absolute* transport between WB2 and the eastern boundary (Fig. 2). For (ii), a time-variable reference transport for the relative $T_{INT}(z)$ needs to be provided. This is achieved by the imposition of a precise compensation among the different flow components, in the sense that the sea surface to sea floor integral of T_{AMOC}(z) yields zero residual mass transport across 26.5°N at each time step, according to

[3] $$\int_{-h_{BOT}}^{0} T_{AMOC}(z) = \int_{-h_{BOT}}^{0} \left[T_{GS}(z) + T_{EK}(z) + T_{MO}(z)\right] \mathrm{d}z = 0 .$$

Kanzow et al. (2007) showed observational evidence for an approximate compensation among the different transport components in [3] over periods in excess of 10 days, using independent bottom pressure measurements. At time scales shorter than 10 days there

are pronounced net barotropic transport fluctuations of ±8 Sv across 26.5°N (see Fig. 2a of Kanzow et al., 2007), which are possibly related to large-scale atmospheric pressure forcing (Bryden et al., 2009). Notable density fluctuations largely compensating for barotropic transports are found at periods in excess of 10 days (Kanzow et al., 2007).

The referencing of $T_{INT}(z)$ is carried out by computing a compensating transport T_C at each time step, as follows

[4] $$T_C = -\int_{-h_{BOT}}^{0} [T_{GS}(z) + T_{EK}(z) + T_{WBW}(z) + T_{INT}(z)]\,\mathrm{d}z$$

It is assumed that the compensating meridional velocity field V_C(x,z) underlying T_C is spatially uniform both in the vertical and zonal domains following model simulations of Hirschi et al. (2003) and Hirschi and Marotzke (2007). Accordingly, $T_C(z) = V_C L(z)$, with L denoting the effective zonal width of the ocean, that decreases with depth. Hence, the absolute mid-ocean transport $T_{MO}(z)$ can be calculated, according to

[5] $$T_{MO}(z) = [T_{\mathrm{INT}}(z) + T_C(z) + T_{WBW}(z)].$$

Finally, the *upper mid-ocean transport* T_{UMO} constitutes that part of $T_{MO}(z)$, that contributes to Ψ^{MAX}, according to

[6] $$T_{UMO} = \int_{-h_{ZC}}^{0} T_{MO}(z)\,.$$

We now limit our analysis and discussion to ten-day low-pass filtered transports, but three main factors may allow for non-zero net mass fluxes across 26.5°N at periods longer than 10 days, namely regional mass storage, external mass sources (net precipitation), and the Arctic throughflow (Bering Strait). The significance of mass storage can be inferred indirectly from bottom pressure measurements. At 26.5°N we observe peak to peak bottom pressure fluctuations of 0.04 dbar and 0.05 dbar at time scales of 20 and 180 days, which exhibit basin-wide correlation scales. If the Atlantic north of 26.5°N displays

coherent mass-changes, this would correspond to uncompensated meridional transports of 0.5 and 0.1 Sv on 20 day and 180 day scales, respectively. For the second two factors, the southward mass transport associated with the Bering Straits flow plus net precipitation between Bering Straits and 26.5°N is thought to vary in time by less than 1 Sv on intra-seasonal time scales (Woodgate and Aagaard, 2005; Wijffels, 2001). Hence, we assume that the net mass (i.e. uncompensated) transport across 26.5°N could be 1.0 Sv rms on 20-day time scales, decreasing to less than 0.5 Sv rms on seasonal time scales. A mass imbalance of 1.0 Sv rms produces an error in the inferred Ψ^{MAX} of 0.2 Sv rms (Appendix B). As we will show later, the fluctuations of Ψ^{MAX} are much larger than this.

c. Isolation of the different transport contributions to the AMOC

It is useful to isolate the contribution of the western and eastern boundaries of the mid-ocean section to fluctuations in Ψ^{MAX}, so that physical mechanisms of density changes at either boundary can be studied separately (Longworth, 2007). For this, $\overline{T}_{GS}(z)$ and $\overline{T}_{EK}(z)$ are fixed in [3] and [4] by using 4-year-average profiles. In addition, to isolate the western boundary contribution to the overturning Ψ^{MAX}_{MOW} (i.e. from the continental slope east of the Bahamas), 4-year-average density profiles $\overline{\rho}_E(z)$, $\overline{\rho}_{MAR1}(z)$ and $\overline{\rho}_{MAR2}(z)$ are used for the computation of $T_{INT}(z)$ in [A1, A3, A4], so that the only contributions to Ψ^{MAX}_{MOW} that vary in time are $T_{WBW}(z)$ and $\rho_W(z)$. Similarly, to isolate the eastern boundary contribution to the time-variable overturning Ψ^{MAX}_{MOE},, 4-year-average density profiles $\overline{\rho}_W(z)$, $\overline{\rho}_{MAR1}(z)$ and $\overline{\rho}_{MAR2}(z)$ are used for the computation of $T_{INT}(z)$ in [A1, A3, A4], so that the only time-variable contribution comes from $\rho_E(z)$. To isolate the overturning transport resulting from the sum of all western boundary transport contributions – hereafter referred to as Ψ^{MAX}_{W} - the time-variable profiles of $T_{WBW}(z)$ and $\rho_W(z)$ and $T_{GS}(z)$ are used together with the time

average profiles of $\overline{T}_{EK}(z)$ $\overline{\rho}_E(z)$, $\overline{\rho}_{MAR1}(z)$ and $\overline{\rho}_{MAR2}(z)$ in the calculations ([3, 4, A1, A3, A4]).

3. Results

a. Vertical structure of the flow field across 26.5°N

The April 2004 – April 2008 mean profile of $T_{AMOC}(z)$ exhibits northward flow between the surface and 1025 m (Fig. 4), which is a combination of the northward transport of 31.7±0.9 Sv of T_{GS} shallower than 780 m (Beal et al., 2008), 3.5±0.8 Sv of T_{EK} shallower than 100 m and 0.9±0.2 Sv of T_{MO} (dashed line) in the Antarctic Intermediate Water (AAIW) range between 660 and 1025 m. The bulk of northward flows are opposed by 17.5±1.4 Sv of southward flow of T_{MO} shallower than 660 m (Fig. 4a), with the latter mostly accounting for the re-circulation within the subtropical gyre but also containing roughly 5 Sv of northward, western boundary flow within the Antilles current (Bryden et al., 2005b). Each of the above error envelopes represents the sum of the standard error and the expected measurement error (Appendix B).

There is 20.7±1.9 Sv of southward flow of NADW between 1025 and 5200 (Fig. 4b). In this layer maximum southward transports are found near 1700 m. A time mean northward transport of 2.1 Sv (Appendix A) at depths larger than 5000 m is prescribed, to approximately account for the unobserved AABW flow (Bryden et al., 2005a), which translates in an uncertainty in the time mean Ψ^{MAX} of less than ±0.2 Sv (Appendix B). Thus, the imposition of a constant AABW transport will only have a small effect on Ψ^{MAX}.

Fig. 5 shows shapshots every five days of the meridional overturning stream function $\Psi(z)$ at 26.5°N (1). The time mean Ψ^{MAX} is 18.7 ±2.1 Sv, with an average zero-crossing depth h_{ZC} at 1025 m, varying by 125 m rms. Note that this result illustrates why a “level of no

motion" assumption associated with the mean depth of a property interface such as the AAIW / NADW interface is potentially inaccurate (Figs. 5 and 6a).

b. Time-variable meridional flow

Figure (7) shows time series of Ψ^{MAX} at 26.5°N and its components. Ψ^{MAX} varies by 4.8 Sv rms (red line) and both it and its components display pronounced intraseasonal and seasonal variability. T_{GS} varies by 2.9 Sv rms, a value representative of the full 1982 – 2008 record of continuous cable measurements (Meinen et al., 2010; Table 1). T_{EK} fluctuates by 3.5 Sv rms and is also representative of longer observational periods (Table 1; Kalnay, 1996). T_{UMO} - representing the vertical integral of $T_{MO}(z)$ between the surface and h_{ZC} (Fig 6a; Eq. 6) - displays fluctuations of 3.2 Sv rms. Since no continuous observations of T_{UMO} were made prior to April 2004, the representativeness of this result can only be assessed indirectly (section 5). The correlations for the transport pairs $<T_{EK},T_{GS}>$, $<T_{EK},T_{UMO}>$ and $<T_{GS},T_{UMO}>$ (0.01, -0.11, and -0.21 respectively) are insignificant at 10 % error probability and hence each of them projects on the variance of Ψ^{MAX}. The correlations for the transport pairs $<\Psi^{MAX},T_{GS}>$, $<\Psi^{MAX},T_{UMO}>$ and $<\Psi^{MAX},T_{EK}>$ are 0.42, 0.43 and 0.62, respectively, and are all significant at 5% error probability. Although T_{EK}, T_{GS} and T_{UMO} vary by roughly the same amount, their frequency distribution displays remarkable differences (Fig. 8). The ageostrophic T_{EK} dominates fluctuations of Ψ^{MAX} at periods between 10 and 90 days , while the seasonal variability of Ψ^{MAX} is dominated by geostrophic (density-balanced) components T_{UMO} and T_{GS}. The contribution to Ψ^{MAX} from the compensation transport $T_C(z)$ at depths shallower than h_{ZC} (grey line in Fig. 7) is ±2.3 Sv, somewhat less than the variability of T_{UMO}, T_{GS} or T_{EK}. As T_C compensates for fluctuations in T_{GS},$T_{EK,}$ and in the observed components of T_{UMO} (i.e., T_{INT} and T_{WBW}; see (5)), it is negatively correlated to all of them (-0.28, -0.41 and -0.42,

respectively).

On seasonal timescales, the 180-day low-pass filtered time series of T_{UMO}, T_{GS} and T_{EK} display fluctuations of 2.2, 1.7 and 1.3 Sv rms, respectively. The sum of the *geostrophic upper-ocean transports* that contribute to Ψ^{MAX} (i.e. T_{UMO} plus T_{GS}) varies by 2.7 Sv rms and clearly dominates over T_{EK}. Moreover, Figure (8) shows that this result is robust over a 26-year time series of T_{GS} and T_{EK} (dashed blue and black lines in Fig. 8).

The separate contributions to Ψ^{MAX} from the western and eastern boundary variability of the mid-ocean section to Ψ_{MOW}^{MAX} and Ψ_{MOE}^{MAX} (see section 2c), fluctuate by 2.3 Sv rms and 2.1 Sv rms, respectively (Fig. 9, black and gray lines), and are uncorrelated.at 10 % error probability. The contribution to Ψ^{MAX} from the western boundary including the Gulf Stream Ψ_{W}^{MAX} (section 2c) fluctuates by 3.0 Sv rms (not shown) and thus exceeds the variability of Ψ_{MOE}^{MAX}. There is a similar picture at seasonal periods (180-day low-pass filtered records), with Ψ_{W}^{MAX}, Ψ_{MOW}^{MAX} and Ψ_{MOE}^{MAX} yielding values of 2.0, 1.4 and 1.3 Sv rms, respectively.

c. Seasonal cycle

Does the Ψ^{MAX} or any of the three upper-ocean contributions exhibit a well-developed seasonal cycle? If so, a prediction of Ψ^{MAX} and of its role in ocean heat storage and meridional heat transport on seasonal time scales might be possible, provided the physics of the forcing are understood. The seasonal cycle of T_{GS} is shown as black solid lines in Fig. 10a (Meinen et al., 2010) and has an amplitude of 3.0 Sv peak-to-peak with a maximum in July and a minimum in November. After 4 years of measurements the seasonal cycle stands out weakly from the mean monthly standard error of ±1.1 Sv (i.e,

the mean monthly standard deviation divided by √4; Table 1), but both amplitude and phase are consistent with the seasonal cycle computed from the 26-year-long time series (dashed line in Fig. 10a).

The seasonal cycle of T_{EK} (Fig. 10b, solid line) has an amplitude of 4.1 Sv peak-to-peak, with a maximum in December and a minimum in March (average standard error ±0.8 Sv). However, month-wise averages do not bring out a seasonal periodicity in T_{EK} (Böning et al., 2001) and the seasonal "cycle" derived from the 4-year record is not representative of the 26 year long record (dashed line in Fig. 10b), which exhibits 2.1 Sv peak-to-peak with a minimum in June and maximum in January. While phase and amplitude of the maximum transport obtained from the long record and the short record are in agreement, the March minimum of the 4-year record is dominated and biased by unusually strong southward flow in March 2005 (Atkinson et al., 2008).

T_{UMO} shows a seasonal cycle of 5.9 Sv peak-to-peak, with a minimum northward transport in April and a maximum one in November (Fig. 10c), clearly significant above the mean monthly standard error of ±1.0 Sv. The seasonal cycle of T_{UMO} is clearly stronger than that of T_{GS} and T_{EK}. The seasonal variability of the vertical profile associated with T_{UMO} is illustrated in Fig 11, where monthly mean profiles of the $T_{MO}(z)$ *anomaly* are shown. Maximum northward flow anomaly occurs in the upper ocean in November, and minimum (relative southward) anomaly occurs in April, consistent with the seasonal cycle of T_{UMO}. Below roughly 1000 m, the pattern is of opposite sign, and the overall variability can therefore be described fundamentally as a first mode-like internal variation of the basin-wide, zonally-averaged interior flow.

Overall, Ψ^{MAX} exhibits variability of 7.8 Sv peak-to-peak, with minimum northward transport in March and maxima in July and November (solid line in Fig. 10d). However, this seasonal cycle of Ψ^{MAX}, is contaminated by the bias in T_{EK} (Fig. 10b) and we can derive a better estimate using the long-term seasonal cycles of the components $T_{EK}^{cycle26y}$ and $T_{GS}^{cycle26y}$ (dashed lines in Fig. 10a and b). Recall, there is no long-term estimate of T_{UMO}, only $T_{UMO}^{cycle4y}$, however this is also contaminated by T_{EK} through the compensation transport T_c, roughly 25 % of which takes place in the upper 1000 m (Fig. 4) . By replacement of the compensation for $T_{EK}^{cycle4y}$ and $T_{GS}^{cycle4y}$ (i.e. 25% of the amplitude) by a compensation for the long-term seasonal cycles ($T_{EK}^{cycle26y}$, $T_{GS}^{cycle26y}$), this contamination can be removed. Accordingly, the long-term seasonal cycle of Ψ^{MAX} is estimated by

[7] $$\Psi^{cycle} = T_{UMO}^{cycle4y} + 0.75\times\left[T_{GS}^{cycle26y} + T_{EK}^{cycle26y}\right] + 0.25\times\left[T_{GS}^{cycle4y} + T_{EK}^{cycle4y}\right],$$

which has an amplitude of 6.7 Sv peak-to-peak with a minimum in March and maxima in July and November (Fig. 10d). The standard error is ±1.2 Sv. The best estimates of the long-term seasonal cycles have been superimposed on the 4 year long transport time series (Fig. 7). For Ψ^{MAX} and T_{UMO} the corresponding seasonal cycles account for a large fraction of the variance , while this is not the case for T_{EK} and T_{GS}.

Fig.12 displays the contributions to Ψ^{cycle} from the western and eastern boundary fluctuations of the mid-ocean section (as shown in Fig. 9). The western boundary signal Ψ_{MOW}^{MAX} (Fig. 12a) has a smaller seasonal cycle with larger uncertainties than the eastern boundary one, Ψ_{MOE}^{MAX} (Fig. 12b) (3.9 versus 5.4 Sv peak-to-peak with standard errors of 1.0 versus 0.5 Sv). Thus, the eastern boundary variability (with a transport minimum in April and maximum in October) dominates the seasonal cycle of T_{UMO}. Chidichimo et al. (2010) also find a coherent seasonal cycle in thermocline eastern margin densities at 26.5°N.

345

4. Causes of mid-ocean seasonal transport cycle

The variability in T_{UMO} is geostrophic, and therefore its seasonal cycle is directly related to the difference in seasonal density anomalies between the eastern and western boundaries. Above we found that the eastern boundary density variability dominates over
350 the western boundary (Fig. 12) and that the seasonal signal in T_{UMO} extends to 1000 m depth (Fig. 11). The latter suggests that the seasonal cycle is not fundamentally related to buoyancy forcing at the ocean surface, but is likely a dynamical response to seasonal wind forcing. Next, we consider a simple model of the forced response of the ocean interior to seasonal wind stress curl variations, focusing on the baroclinic response, to try to attribute
355 a mechanism to the observations.

The linear, sub-inertial response of a stratified ocean to wind-stress curl variability can be expressed in terms of vertical modes $\Phi_n(z)$, whose time and zonally-varying amplitude $p_n(x,t)$ is given by (Anderson and Gill, 1975; Sturges et al, 1998):

360 [8] $$\frac{\partial p_n}{\partial t} - \beta c_n^{\,2} f^{-2} \cdot \frac{\partial p_n}{\partial x} = -c_n^{\,2} f^{-1} \cdot G_n \nabla \times \tau$$

where β is the planetary vorticity gradient ($\partial f/\partial y$), c_n is the long Rossby wave speed for the nth vertical mode, and G_n is an amplitude factor governing the projection of the forcing onto the vertical modes:

365 [9] $$G_n = H_{mix}^{-1} \cdot \int_{-H_{MIX}}^{0} \Phi_n(z)\,\mathrm{d}z \Big/ \int_{-H}^{0} \Phi_n(z)^2\,\mathrm{d}z$$

where H_{mix} is the mixed layer depth.

We calculated vertical modes $\Phi_n(z)$ and associated c_n from climatological (Levitus, 1982) hydrographic data along 26.5°N and chose the results from a representative longitude (60°W) for the calculation. [8] was solved in a forward time-stepping mode from zero initial conditions using the climatological seasonal cycle of wind stress curl anomaly across 26.5°N (Fig. 13a) extracted from the Scatterometer Climatology of Ocean Winds (SCOW; Risien and Chelton, 2008). The equilibrium seasonal cycle of p_n across the basin then results in a basin-wide mid-ocean geostrophic transport anomaly for each mode of:

[10] $$T_{MO_n}^{\nabla\times\tau}(z) = \int_{X_W}^{X_E} v_n(z)dx = \int_{X_W}^{X_E} (\rho f)^{-1} \frac{\partial p_n}{\partial x} \Phi_n(z)dx = (\rho f)^{-1} \Phi_n(z)[p_n(x_E) - p_n(x_W)]$$

The seasonal cycle of $p_n(x_E)$ is given simply by the locally-forced solution at the eastern boundary. The western boundary signal $p_n(x_W)$ represents the locally-forced solution at the western boundary plus accumulated effects of Rossby wave propagation from forcing west of the Mid-Atlantic Ridge at 50°W , since studies indicate that the MAR effectively blocks propagation of baroclinic Rossby waves from the eastern basin (Barnier, 1988; Herrmann and Krauss, 1989, Osychny and Cornillon, 2004).

The seasonal wind stress curl anomaly along 26.5°N (Fig. 13a) has a semi-annual cycle over most of the basin. The largest signal, however, occurs at the eastern boundary, which is annual in nature with a pronounced anticyclonic curl anomaly in summer and cyclonic anomaly in winter (Fig. 13a, b). It is caused by strong summertime intensification of northerly winds adjacent to the eastern boundary, and their relaxation in winter.

Fig. 14a shows the resulting model predicted variation of the mid-ocean transport profile across the basin, $T_{MO}^{\nabla\times\tau}(z)$ - computed according to [8-10] - where we have summed the response of the first two baroclinic modes, with H_{mix} = 100 m (higher baroclinic modes

have a negligible contribution). There is a good correspondence between the observed interior $T_{MO}(z)$ seasonal cycle and the model prediction (Fig. 10). The seasonal AMOC anomaly associated with the model-predicted mid ocean transport $T_{UMO}^{\nabla\times\tau}$ (calculated as the upper ocean transport anomaly) is approximately 4.3 Sv peak-to-peak (Fig. 14b, blue line) and its amplitude and phase are comparable to that of the observed T_{UMO} seasonal cycle (5.9 Sv) of Fig. 10c. The model suggests that this response is due almost entirely to internal pressure variations at the eastern boundary (Fig 14b, green line), which, in turn, are due to the dominance of the wind stress curl signal at the eastern boundary (Fig. 13a,b). There is a good agreement between the model's eastern boundary seasonal transport cycle of 4.2 Sv peak-to-peak and the observed eastern boundary contribution Ψ_{MOE}^{MAX} (Fig. 12b) both in amplitude (5.4 Sv) and in phase (maximum / minimum northward transport October / April). Essentially, the model implies that the seasonal variation of the zonally-integrated interior flow profile is almost entirely attributable to changes in stratification at the eastern boundary, caused by local wind stress curl variations that uplift (depress) density surfaces in the spring (fall), which follow, in quadrature, the winter (summer) periods of enhanced cyclonic (anticyclonic) curl at the eastern boundary.

While largely consistent with the basin-wide integrated flow, the simple linear wave model has many limitations. It only allows for purely zonal propagation of northward transport anomalies. It also does not include the effect of horizontal mean flow (and vertical shear) on the anomalies, nor the impact of topography, as anomalies generated on the eastern boundary move westward (e.g. Killworth and Blundell, 2005). It can therefore not be expected to give an accurate description of the zonal distribution of northward flows in the basin interior along 26.5°N.

The mid-ocean variability predicted by the model is distinct from the quasi-stationary topographic Sverdup response of the ocean interior to the wind stress curl forcing, which depends on the zonally-integrated wind stress curl across the entire basin. It is well established from theory and models (Anderson and Gill, 1975, Anderson and Corry, 1985) and observations (Lee et al., 1996) that on seasonal time scales, this response is carried primarily in the barotropic mode. This circulation is essentially transparent to our array, and has no effect on Ψ^{MAX}. The *baroclinic* response of the interior depends on the density differences between the eastern and western boundaries, which instead are related to first order to the *differences* in wind stress curl forcing at the eastern and western boundaries, which are the fundamental dynamics expressed in the above model.

5. Discussion

a. Seasonal cycle

From a global perspective, the seasonal anomalies of Ψ^{MAX} are thought to be dominated by fluctuations of the Ekman transport, compensated for by a nearly depth-independent geostrophic return flow below the Ekman layer (Jayne and Marotzke, 2001; Böning et al., 2001; Wunsch and Heimbach, 2009). Jayne and Marotzke (2001) point out that the seasonal cycle of the northward Ekman transport and of the meridional overturning circulation are on average symmetric about the equator with nodes at the equator, and 20° north and south of it. We have shown that T_{GS} and T_{UMO} exceed T_{EK} in terms of both amplitude of the seasonal cycle and rms fluctuations on seasonal time scales. The mostly geostrophic seasonal cycle of T_{UMO} of 5.9 Sv peak-to-peak at 26.5°N is comparable in amplitude with the maximum seasonal cycles of T_{EK} in the North Atlantic, which are found in the tropics (10 Sv) and at mid-latitudes (6 Sv). One might therefore speculate that

throughout the Atlantic the contribution of geostrophic upper-ocean transports to seasonal anomalies of Ψ^{MAX} might be comparable to that of T_{EK} (Hirschi et al., 2007). This is consistent with repeated hydrographic observations at 35°S in the Atlantic (Baringer and Garzoli, 2007; Garzoli and Baringer, 2007).

Our measurements suggest that the largest part of the seasonal cycle of T_{UMO} is driven by density anomalies at the eastern boundary of the Atlantic. Chidichimo et al. (2010) find coherent seasonal anomalies in density in the depth range between 100 m and 1400 m at the mooring sites on the upper continental slope of the eastern boundary while 1000 km offshore no significant seasonal density anomalies are found at depths in excess of 100 m. It is therefore plausible that the transport anomalies which dominate the seasonal cycle of T_{UMO} do not correspond to basin-scale coherent flows but are rather concentrated in a narrow band along the eastern boundary. This concept is consistent with the observed near-eastern-boundary intensification of the seasonal wind stress curl anomalies.

b. Wind stress curl forcing of seasonal anomalies of Ψ^{MAX}

The response of T_{UMO} to the seasonal cycle in wind stress curl along 26.5°N has been simulated in a linear "Rossby wave model" which implies that the seasonal variation of T_{UMO} is almost entirely attributable to changes in stratification at the eastern boundary, caused by local wind stress curl variations. Orography, sea surface temperature gradients and ocean currents are known to affect wind stress curl (Chelton et al., 2004), as (i) constrictions due to sloping continental orography, island tips and inter-island gaps create jet winds, and (ii) differential heating of the marine atmospheric boundary layer across an SST front accelerates wind over warm waters and decelerates it over the cold waters. In the annual mean fields there is a narrow band of coherent positive wind stress curl along

the eastern margin of the Atlantic from south of Cape Vert near 15°N to Cape Finisterre near 43°N, (Fig. 2 of Chelton et al., 2004).

Ongoing studies based on Quickscat data suggest that seasonal anomalies in wind stress curl in the tropical / subtropical Atlantic are meridionally coherent (1000 km scale) along the eastern boundary (not shown), but with rather small zonal scales, and may be related to a seasonal pattern with alternating signs in the zonal direction extending westward from the coast to about 19.5°W resulting from orographic jet winds induced by the Canary islands and Cape Yubi (at 28°N on the Moroccan coast). Hence, we expect the seasonality in T_{UMO} at 26.5°N to have a large meridional coherence scale, modulated locally by jet winds. It has been demonstrated that orography, SST gradient and ocean current effects on the wind stress curl along continental margins are poorly represented in data sets such as the NCEP/NCAR reanalysis (Chelton et al., 2004) that are routinely used to drive ocean models. Yet our Rossby wave model suggests that these effects may drive the seasonal cycle in the circulation. Kanzow et al. (2009) showed that an eddy resolving (1/12°) numerical model significantly underestimated the variability of T_{UMO} at 26.5°N due to unrealistically small density fluctuations at the ocean margins. If this is a general problem of even high-resolution, eddy-resolving numerical models, the true impact of *upper-ocean geostrophic transports* (i.e. the sum of T_{UMO} and T_{GS}) on intra-seasonal to seasonal variations of Ψ^{MAX} may be much larger than model simulations imply. Fennel and Lass (2007) argue that realistic wind stress curls along ocean margins are required to realistically simulate the vertical structure of the near coastal thermocline and currents in ocean models. The mechanism of near boundary seasonal wind-stress curl anomalies effecting T_{UMO} via local uplift / depression of isopycnals (Köhl et al., 2005; Chidichimo et al., 2010) is reminiscent of a mechanism of multi-annual variability of T_{UMO} in the

subtropical North Atlantic as recently proposed by Cabanes et al. (2008).

c. *Is the variability in Ψ^{MAX} observed between April 2004 and April 2008 representative of longer time periods?*

Neither is there nor has there been any other AMOC observing system in place to compare our results to. Therefore the long-term representativeness (particularly of T_{UMO}) can only be assessed indirectly. A large body of literature exists on hydrographic variability on intra-seasonal to decadal periods in the North Atlantic (e.g. Roemmich and Wunsch, 1985; Joyce and Robbins, 1996; Joyce et al., 1999; Johnson and Gruber, 2007; Cunningham and Alderson, 2007; Kieke et al, 2009). However, there is no straightforward link between changes in hydrographic properties and changes in Ψ^{MAX}. For example, the strength of the AMOC-related Labrador Sea outflow along the western boundary appears to have been stable despite a decade-long warming trend in the outflow waters (e.g., Schott et al., 2006). A further complication for the interpretation of historical hydrographic data in terms of Ψ^{MAX} is that density measurements away from the ocean boundaries (even few tens of kilometers away), do not provide a strong constraint on AMOC transport variability at 26.5°N (Kanzow et al., 2009) due to eddy-noise.

Unfortunately, a similar limitation applies to satellite altimetry data which otherwise could be considered as a promising way to extend our timeseries back in time. Kanzow et al. (2009) have shown that sea surface height (SSH) differences between the eastern and western boundary cannot be used to infer the temporal variability of T_{UMO} at 26.5°N. They argue that this is primarily due to the more complex vertical structure of the flow close to the ocean boundaries which inhibits a simple projection of SSH on the first baroclinic mode

(in contrast to the offshore ocean). The results are in agreement with simulations based on a numerical model by Hirschi et al. (2009).

Currently, simulations from numerical models are probably the only source for long, daily AMOC timeseries exceeding our 4-year measurement period. In their ocean state estimate Wunsch and Heimbach (2009) find a dominant seasonal tropical Ekman transport response which is in line with the results of Jayne and Marotzke (2001). Whether the state estimate successfully captures the observed seasonal anomaly in T_{UMO} at 26.5°N is unclear. In general, the degree of realism of fluctuations in T_{UMO} in assimilation products will depend (among other things) on purposeful observations which provide strong constraints on the basin-wide integrated northward flow. Hydrographic measurements away from the ocean boundaries or SSH do not fall in this category (Kanzow et al., 2009). This view is supported by findings of Smith et al. (2009, manuscript submitted) who show that the assimilation of hydrographic data from ARGO floats into a numerical model fails to improve the temporal variability of Ψ^{MAX}, when compared with the RAPID-MOC / MOCHA time series. They conclude that density measurements across the ocean margins are required to constrain the flow. The scarcity of such observations might also explain why today's state-of-the-art ocean state estimates (even when carefully constrained by the same observations) remarkably differ from one another in terms of the strength and temporal variability of Ψ^{MAX} (Lee, 2009).

In this study wind stress curl at the eastern boundary has been identified as a possible driving mechanism of the seasonal cycle of T_{UMO}. Assuming that this relationship is robust, the representativeness of the seasonal cycle in T_{UMO} (derived from the 4 year measurement period) of longer measurement intervals will be linked to the

representativeness of the seasonal cycle of the wind stress curl. The Quickscat high-resolution wind measurements started in 1999. From daily gridded wind stress data (horizontal resolution of 0.25° x 0.25°) the monthly mean wind stress curl was computed close to upper-ocean density moorings (EBH4, EBH5). Fig. 15 reveals that the seasonal cycle is a rather regular feature at the eastern boundary over the 12 year interval, both in phase and in amplitude. It clearly dominates the variability at this location, as each of the January values in the 1999 to 2009 interval are larger than each of the July ones. In addition, the seasonal cycle in wind stress curl from the 2004 – 2008 interval (bold dashed line) is almost identical to that from the 1999 – 2009 interval (bold solid line). The observed seasonal cycle of T_{UMO} may therefore be representative of the last decade and even longer periods.

If the seasonal cycle of T_{UMO} is a long-term persistent feature of the ocean circulation at 26.5°N, it is likely that the inference of decadal trends in Ψ^{MAX} based on hydrographic snapshots might suffer from seasonal biases. Bryden et al. (2005a) deduced a decline in Ψ^{MAX} of 8 Sv between 1957 and 2004 using the 5 hydrographic sections shown in Fig. 16 (filled squares and Table 2). They used constant values for T_{EK} and T_{GS}, leaving T_{UMO} as the only time-variable component of Ψ^{MAX}. Based on our analysis, the months of the first and last cruises (October and April) correspond to the maximum and minimum in the seasonal cycle of T_{UMO} (Fig. 10c), such that the 1957 and 2004 estimates are likely to be biased high and low, respectively. If we subtract the seasonal anomalies of T_{UMO} (shown in Fig. 10c) from the hydrographic estimates, by taking into account the months in which the cruises were conducted (Table 2), the resulting "de-seasoned" time series of Ψ^{MAX} (open diamonds Fig. 16) exhibits a reduction in variance of more than 80% and does not show a persistent decline. The efficiency of the seasonal bias correction in removing variance

implies that aliasing due to seasonal anomalies possibly accounts for a large part of the trend found by Bryden et al. (2005a).

d. What are the meridional scales associated with the seasonal anomalies?

In the climate context, it would be instructive to know what the meridional scales of the seasonal anomalies in Ψ^{MAX} (and of the associated meridional heat transport) are. Are the seasonal anomalies a local phenomenon (i.e., associated with an eddy de-correlation scale of O(100 km) or less), or is their meridional extent of O(1000 km)? To answer this question, simultaneous continuous measurements of density along the ocean margins at different latitudes and depth levels would be required. As mentioned above such observations are very rare and this represents a major gap in today's ocean observing system.

A handle on the meridional scales of anomalies in T_{UMO} (or Ψ^{MAX}) may indirectly be obtained from numerical models and / or plausibility arguments. Kanzow et al. (2009) concluded from a combination of RAPID-MOC / MOCHA observations, altimetry and a high-resolution numerical model, that the impact of local eddies on T_{UMO} at 26.5°N was rather small. Numerical model results from Hirschi et al. (2007) relying on monthly values suggest that anomalies of the *thermal wind* component of Ψ^{MAX} (i.e. the Ekman and external component subtracted) at 26.5° display a meridional de-correlation scales of roughly 1000 km.

Numerical models have shown that Ψ^{MAX} at low latitudes in the Atlantic (including 26.5°N) is highly correlated with the advective meridional heat transport (e.g., Böning et al., 2001;

Kanzow et al., 2008b), and this has been confirmed from an analysis of the RAPID-MOC / MOCHA measurements (Johns et al., 2010; in preparation). Further, it has been shown that the meridional divergence of advective meridional heat transport nearly balances upper ocean heat storage on seasonal time scales at low latitudes, whereas towards higher latitudes air-sea heat fluxes are of primary importance (e.g. Jayne and Marotzke, 2001). This study suggests that seasonal geostrophic upper-ocean transport fluctuations are stronger than previously thought. Therefore the possible meridional divergence of these might represent an important contribution to low-latitude, seasonal heat storage anomalies.

Johns et al. (2010; in prep.) find that a change in Ψ^{MAX} of 1 Sv at 26.5°N corresponds to a change in advective heat transport of $0.06 \cdot 10^{15}$ W. A simple calculation shows that meridional divergence in upper-ocean geostrophic flow of 2 Sv between two transatlantic sections separated by 1000 km over the course of 6 months would lead to a net temperature change of 0.2°C in the upper 500 m (if there is no exchange with the atmosphere). Since heat storage will not be spatially uniform, local changes (near the ocean margins) larger than this on seasonal periods are likely. In contrast anomalous T_{UMO} associated with an eddy scale of O(100 km) would correspond to a 2°C anomaly, which is far more than we observe at the various measurement sites. From these considerations we assume that the meridional extent of the seasonal anomalies is likely to be of O(1000 km) rather than being set by localized eddy processes.

Possible seasonal storage of heat by large-scale divergences of geostrophic upper-ocean transport may be important for regional oceanic - and of near-boundary continental climates, if the heat is (partly) released to the atmosphere. Near-surface seasonal heat

storage at low latitudes may represent a non-negligible source of energy for tropical cyclones. However, given that wind stress curl forcing along coastal margins may be unrealistically small in OGCMs, simultaneous, continuous observations of upper-ocean geostrophic transport across two or more zonal transects would be needed to observe the possible existence of strong upper-ocean meridional geostrophic transport divergence.

6. Conclusions

- Between April 2004 and April 2008 the strength of the AMOC, Ψ_{MAX}, at 26.5°N has a mean of 18.7 ±2.1 Sv and rms fluctuations of 4.8 Sv. At periods shorter than 100 days T_{EK} variability dominates over T_{GS} and T_{UMO} , while at seasonal time scales Ψ^{MAX} variability is dominated by T_{UMO} and T_{GS}.
- The total western boundary contribution Ψ_{W}^{MAX} (i.e. T_{GS} plus western boundary contribution of the upper-mid-ocean component Ψ_{MOW}^{MAX}) to "seasonal variability" (180 day low-passed) is significantly larger than that of the eastern boundary Ψ_{MOE}^{MAX} (2.0 Sv versus 1.3 Sv rms).
- The best estimate of the long-term peak-to-peak amplitude of the seasonal cycle of Ψ^{MAX} is 6.7 Sv. From the three transport components T_{UMO} has the most pronounced seasonal cycle of 5.9 Sv peak-to-peak with a maximum northward upper-ocean transport in autumn and a minimum in spring. The T_{UMO} cycle is dominated by the density contribution from the eastern boundary which has a peak-to-peak amplitude of 5.4 Sv.
- The response of T_{UMO} to the seasonal cycle in wind stress curl along 26.5°N has been simulated in a linear "Rossby wave model". The modelled and observed seasonal cycle of T_{UMO} agree both in phase and amplitude. The model implies that the seasonal variation of T_{UMO} is almost entirely attributable to changes in

stratification at the eastern boundary, caused by local wind stress curl variations that uplift (depress) density surfaces in the spring (fall), which follow, in quadrature, the winter (summer) periods of enhanced cyclonic (anticyclonic) curl at the eastern boundary.

Acknowledgements

The authors would like to thank the captains and crews of the research vessels Charles Darwin, Discovery, Ronald H. Brown, Knorr, Poseidon and Seward Johnson, and the UKORS, RSMAS and AOML mooring and hydrography teams. The mooring operations have been supported by the National Environmental Research Council (NERC) RAPID programme, the US National Science Foundation (NSF) under grant number 0728108, and the US National Oceanic and Atmospheric Administration (NOAA) Western Boundary Time Series program. The Florida Current cable data are made freely available by the Atlantic Oceanographic and Meteorological Laboratory (www.aoml.noaa.gov/phod/floridacurrent/) and are funded by the NOAA Office of Climate Observations. The wind stress data were obtained from CERSAT, at IFREMER, Plouzané (France). We would like to thank Darren Rayner (NOCS) for coordinating the UK seagoing activities and leading the mooring data recovery. Two of the authors (TK, JJMH) were supported in the framework of the NERC funded Rapid Climate Change Programme (Grant 880 NER/T/S/2002/00481). We would like to thank the two anonymous reviewers for their detailed criticism which lead to significant improvement of the manuscript.

Appendix A: Computation of internal transport T_{INT}

In the following we describe how the northward geostrophic internal transport T_{INT} (that is required to estimate T_{MO} [5]) is computed. This study differs from the approach taken by Cunningham et al. (2007) and Kanzow et al. (2007) in two ways. Firstly, density measurements from both the eastern and western flanks of the MAR (Fig. 2) are included in the calculations to be able to account for potential pressure gradients across it, as the AABW piles up against the western flank of the MAR. Mooring MAR1 (on the western MAR flank) gives a density profile over the whole water column, whereas MAR2 (on the eastern flank) covers the 2500 – 5000 m range. Accordingly, we can split $T_{INT}(z)$ into a western (T_{INT_W}) and eastern (T_{INT_E}) basin contribution. In the upper 4740 m of the water column T_{INT_W} is computed from the density difference between MAR1 and WB2 (rel. to -4740 m), according to

[A1] $T_{INT\_W}(z) = -g/(f\rho)\int_{z_{REF}}^{0}[\rho_{MAR1}(z') - \rho_W(z')]dz$, for z < 4740 m.

The second difference to Cunningham et al. (2007) and Kanzow et al. (2007), is that we account for the net northward transport in the AABW layer (McCartney and Curry, 1993; Bryden et al., 2005a), that is not part of the measurement campaign. This way, comparisons of the magnitude of Ψ^{MAX} between hydrography-derived estimates including the AABW range (Bryden et al., 2005a), and this study, are free from potential biases resulting from different vertical ranges of the underlying transport profiles. $T_{INT\_W}(z,t)$ is extended in the vertical to 6000 m with a time-invariant AABW transport-per-unit-depth profile $T_{AABW}(z)$, as shown in Fig. A1. The latter represents a smoothed approximation of 5 historical transport profiles across 26.5°N, as estimated from hydrographic measurements (Bryden et al., 2005a). $T_{AABW}(z)$ spans the 5000 – 6000 m depth range. An offset c is added to the $T_{AABW}(z)$ profile such that finally a time mean northward transport of $T_{AMOC}(z)$ of 2.1 Sv at depths exceeding 5000 m is obtained, representing the average of the 5

estimates from Bryden et al. (2005a),

[A2] $T_{INT\_W}(z,t) = T_{AABW}(z) + c$; for 5000 m < z < 6000 m

The gap between 4740 and 5000 m is filled by vertical interpolation (using a cubic spline) between the time mean of $T_{INT\_W}(z)$ above 4740 m and below 5000 m, ensuring a smooth transition. Hence, for z > 4740 m $T_{INT\_W}(z)$ is time-invariant.

At 26.5° N the MAR crest height is at about 2500 m. Major deep trenches such as the Romanche (Equator), Vema (11°N) and Kane (24°N) Fracture Zones cut though the MAR and thus allow for a zonal exchange of deep and bottom waters in excess of 3700 m (Mercier and Speer, 1998). At depths greater than the intermediate water level, isotherms along 26.5°N spread almost horizontally across the basin up to a depth of 3700m. Below that northward transport of AABW manifests itself in an upward slope of western basin isotherms towards the MAR. Consequently, we assume that the MAR is permeable at depths shallower than 3700 m. Based on this, $T_{INT\_E}(z,t)$ is computed as follows. In the 3700 - 4740 m range transports are computed from the density difference between the eastern boundary and MAR2 (rel. 4740 m):

[A3] $T_{INT\_E}(z) = -g/(f\rho)\int_{-4740}^{-3700}[\rho_E(z') - \rho_{MAR2}(z')]dz$ for -4740 m < z <= - 3700 m.

Shallower than 3700 m $T_{INT\_E}(z,t)$ is obtained from the eastern boundary to MAR1 density difference relative to the time-variable value of T_{INT_E} (z = -3700 m) as derived from [A3].

[A4] $T_{INT\_E}(z) = -g/(f\rho)\int_{-3700}^{0}[\rho_E(z') - \rho_{MAR1}(z')]dz + T_{INT\_E}(-3700)$, for z >= 3700 m.

We assume there is no vertical shear in $T_{INT\_E}(z,t)$ below 4740 m, accordingly

[A5] $T_{INT\_E}(z,t)$ = 0 for z < -4740 m.

$T_{INT}(z)$ integrated between the western boundary (WB2) and the eastern boundary is then given by the sum of the eastern and western contributions, according to

[A6] $T_{INT}(z)$ = $T_{INT\_W}(z)$ + $T_{INT\_E}(z)$.

Appendix B: Error bars

Uncertainties in time mean transports can come from 3 sources: (i) measurement errors (temperature, conductivity, velocity, wind stress, cable voltage), (ii) model errors (e.g. geostrophic approximation; compensation), and (iii) the time variability of the transport signal (standard errors). The measurement errors consist of two parts, random errors, and possible bias errors. A detailed error analysis for a precursor experiment near 26.5°N (Johns et al., 2005; Kanzow et al., 2006) has an error in baroclinic transports (i.e. T_{INT}) of 2.5 Sv rms. The precursor experiment used a lower number of vertical density sampling levels, less precise temperature sensors, and very few pressure measurements and no conductivity measurements. Based on this we estimate the error in instantaneous (i.e. 10-day low-pass filtered) measurements of top-to-bottom integrated $T_{INT}(z)$ is less than 2.0 Sv rms. The contribution of the instantaneous uncertainty in T_{INT} to that of Ψ^{MAX} will be less than 1.5 Sv rms, as a result of the application mass compensation (reduction of 25%). The errors in T_{INT} arise from both uncertainties in the *T*, *C* and *P* sensors, and vertical interpolation between the discrete measurement levels. As the sensors are replaced and carefully calibrated each year, potential biases in the 4-year average sensor-related uncertainties are expected to be small. The interpolation-related uncertainty is mostly random, even if the sampling levels do not change over time [see Fig. 18 of Johns et al. (2005)]. Therefore, the uncertainty of the 4-year-mean will be substantially smaller than the instantaneous uncertainty. We therefore expect the remaining four-year-mean bias of Ψ^{MAX} (and T_{UMO}) resulting from uncertainties in T_{INT} to be not larger than ± 1.0 Sv.

Errors in daily mean instantaneous (3-day low-pass filtered) measurements of T_{GS} amount to 1.7 Sv rms with the errors being mostly random (Larsen, 1992; Meinen et al., 2010). T_{GS} is regularly corrected for potential biases using independent estimates of T_{GS} from

calibration cruises (relying on velocity measurements from dropsondes). A conservative estimate of the four year averaged uncertainty in T_{GS} is ± 0.5 Sv. This is based on the fact that 6 or more cable calibration cruises per year are performed on average, yielding over 24 independent calibration points over the 4 year record, each with ±1.7 Sv accuracy, and therefore a mean transport bias of $1.7/\sqrt{24} = 0.3$ Sv. We estimate the possible 4 year mean bias in T_{EK} is ±0.5 Sv (resulting from uncertainties in both wind measurements and the drag coefficient). We consider this estimate to be rather conservative as (i) it amounts to 15% of the observed time mean of T_{EK}, and (ii) rms differences in T_{EK} between instantaneous values from Quickscat and NCEP / NCAR amount to 0.5 Sv rms. The instantaneous error in T_{WBW} yields 0.4 Sv rms (including possible mean biases), based on comparisons between lowered acoustic Doppler and the moored current measurements at the western boundary for T_{WBW}. The four year mean bias of T_{WBW} should be of O(±0.2 Sv).

Instantaneous measurements of T_{AABW} do not exist, and so the uncertainty of both instantaneous and time mean values is difficult to estimate. The standard deviation of the 5 snapshot estimates of AABW transport at 26°N (Bryden et al., 2005a) is 0.5 Sv. The true uncertainty instantaneous measurements of T_{AABW} might be somewhat larger due to possible undersampling of the deep transport signal over rough bathymetry (Ganachaud, 2003), say, less than 1.0 Sv rms. The impact of a 1.0 Sv uncertainty in T_{AABW} to that in Ψ^{MAX} is less than 0.2 Sv rms. This is because compensation transport $T_C(z)$ (see [4]) is essentially barotropic, so that the compensation for the error contribution of T_{AABW} is distributed almost uniformly in the vertical. As Ψ^{MAX} is an integral over approximately the upper 1000m and the average depth of the section is around 5000m, the errors contributing to Ψ^{MAX} amounts to only about 20% of the uncertainty in T_{AABW}. Therefore the 4 year average bias in Ψ^{MAX} from this contribution should be less than 0.2 Sv. If there is a

mean 1 Sv net transport across 26.5°N resulting from the inflow into the Arctic through Bering Strait, this can only show up in our array as barotropic component (since all vertically sheared flow is accounted for in T_{INT}). If one added this to the observed (mass-balanced) profile, and integrated from the surface downward to h_{ZC}, it would add an uncertainty to Ψ^{MAX} of about 0.2 Sv (or 20% of 1 Sv).

Combining the above error estimates as root-sum-square, we estimate the measurement error for the four year average of Ψ^{MAX} is ± 1.3 Sv (from rms errors of T_{INT} 1.0 Sv, T_{GS} 0.5 Sv, T_{EK} 0.5 Sv, T_{WBW} 0.2 Sv, T_{AABW} 0.2 Sv, and Bering Strait imbalance 0.2 Sv).

It is beyond the scope of this paper to discuss the model related errors. Scaling arguments imply that the errors in using the geostrophic and Ekman approximations for our application are on the order of 3% (Kanzow, 2000). The standard error of a time series can be estimated as the standard deviation divided by the square-root equivalent degrees of freedom (DOF). To estimate the DOF we divide the timeseries length by the integral timescale. We define the integral time scale as the sum of the autocorrelation from minus zero crossing to plus zero crossing (Tennekes and Lumley, 1972). The results are summarized in Table 1. Division of the observational period of 1450 days by the integral time scale then gives the DOF. The standard errors of Ψ^{MAX}, T_{GS}, T_{EK} and T_{UMO} amount to 0.8, 0.4, 0.3 and 0.6 Sv, respectively.

Therefore the total uncertainty of the four year mean Ψ^{MAX} (representing the sum of the measurement error and standard errors) amounts to 1.3 Sv + 0.8 Sv = 2.1 Sv. In principle the two errors cold also be combined randomly, since they have arbitrary signs, but we choose to add them linearly.

References

Anderson, D.L.T. and A.E. Gill, 1975. Spin-up of a stratified ocean with application to upwelling. *Deep-Sea Res. I*, **22**, 583-596.

Anderson, D.L.T., and R.A. Corry, 1985: Seasonal transport variations in the Florida Current: A model study. *J. Phys. Oceanogr.*, **15**, 773-786.

Atkinson, C.P., H.L. Bryden, and T. Kanzow, 2008: Ekman Transport Variability at 26°N in the Atlantic. *Poster presentation at the Rapid Climate Change 2008 annual meeting, Cambridge, UK (www.noc.soton.ac.uk/rapid/sci/viewabs1.php?keyword1=bqw336).*

Baringer, M.O., and S.L. Garzoli, 2007: Meridional heat transport determined with expendable bathythermographs part I: Error estimates from model and hydrographic data. *Deep-Sea Res. I,,* ***54***(8), doi:10.1016/j.dsr.2007.04.013, 1390-1401.

Baringer, M.O., W.E. Johns, C.S. Meinen, D. Shoosmith, H.L. Bryden, 2008: On the Structure of Florida Current Variability. *Poster presentation at the Rapid Climate Change 2008 annual meeting, Cambridge, UK (http://www.noc.soton.ac.uk/rapid/sci/viewabs1.php?keyword1=gwa806).*

Barnier, B., 1988: A numerical study on the influence of the Mid-Atlantic Ridge on nonlinear first-mode baroclinic Rossby waves generated by seasonal winds. *J . Phys. Oceanogr.*, **18,** 417-433.

Beal L. M., J. M. Hummon, E. Williams, O. B. Brown, W. Baringer, E. J. Kearns, 2008: Five years of Florida Current structure and transport from the Royal Caribbean Cruise Ship Explorer of the Seas. *J. Geophys. Res.*, **113**, C06001, doi:10.1029/2007JC004154.

Biastoch, A. and Böning, C. W. and Getzlaff, J., 2008: Causes of Interannual-Decadal Variability in the Meridional Overturning Circulation of the Midlatitude North Atlantic Ocean. *J. Clim.*, **21**, 6599, doi:10.1175/2008JCI2404.1

Bryden, H. L., H. L. Longworth, and S. A. Cunningham, 2005a: Slowing of the Atlantic Meridional Overturning Circulation at 25°N. *Nature*, **438**, 655-657.

Bryden, H. L., W. E. Johns, and P. M. Saunders, 2005b: Deep western boundary current east of Abaco: Mean structure and transport, *J. Mar. Res.*, **63**, 35-57.

Bryden, H. L., A. Mujahid, S. A. Cunningham and T. Kanzow. 2009: Adjustment of the Basin-Scale Circulation at 26°N to Variations in Gulf Stream, Deep Western Boundary Current and Ekman Transports as observed by the Rapid Array, Ocean Science, 5, 421-433.

Böning, C. W. ; Dieterich, C. ; Barnier, B. ; Jia, Y., 2001: Seasonal cycle of meridional heat transport in the subtropical North Atlantic: a model intercomparison in relation to observations near 25N . *Progr. Oceanogr.*, **48**, 231-254

Cabanes, C., T. Lee, and L.-L. Fu, 2008: Mechanisms of interannual variations of the meridional overturning circulation of the North Atlantic Ocean. *J. Phy. Oceanogr.*, **38**, 467-480.

Chelton, D. B., M. G. Schlax, M. H. Freilich and R. F. Milliff, 2004: Satellite measurements reveal persistent small-scale features in ocean winds. *Science*, **303**, 978-983.

Chidichimo, M. P., Kanzow, T., Cunningham, S. A., and Marotzke, J., 2010: The contribution of eastern-boundary density variations to the Atlantic meridional overturning circulation at 26.5° N, *Ocean Sci.*., 6, 475-490.

Cunningham, S.A., Alderson, S. 2007:Transatlantic temperature and salinity changes at 24.5°N from 1957 to 2004. *Geophysical Research Letters* 34 (14), art. no. L14606

Cunningham, S. A., T. O. Kanzow, D. Rayner, M. O. Barringer, W. E. Johns, J. Marotzke, H. R. Longworth, E. M. Grant, J. J.-M. Hirschi, L. M. Beal, C. S. Meinen, and H. L. Bryden, 2007: Temporal variability of the Atlantic Meridional Overturning Circulation at 26.5°N. *Science*, **317,** 935-938.

Delworth, T., S. Manabe, R. J. Stouffer, 1993: Interdecadal variations of the thermohaline circulation in a coupled ocean-atmosphere model. *Journal of Climate,* **6**, 1993-2011.

Fennel, W., and H. U. Lass, 2007: On the impact of wind curls on coastal currents. *J. Mar. Syst.*, **68**, 128 - 142

Ganachaud, A., 2003: Error budget of inverse box models: The North Atlantic. *J. Atmos. Ocean. Tech.*, **20,** 1641-1655.

Ganachaud, A., and C. Wunsch, 2003: Large-scale mass transports, water mass formation, and diffusivities estimated from World Ocean Circulation Experiment (WOCE) hydrographic data. *J. Geophys. Res.*, **108**, 3213, doi: 3210.1029/2002JC001565.

Garzoli, S.L. and M.O. Baringer, 2007: Meridional heat transport determined with expandable bathythermographs Part II: South Atlantic Transport. *Deep-Sea Res. I,* **54**(8), DOI: 10.1016/j.dsr.2007.04.013, 1402-1420.

Hall, M. M., and H. L. Bryden, 1982: Direct estimates and mechanisms of ocean heat transport. *Deep-Sea Res.*, **29**(*3A*), *339-359*.

Herrmann, P., and W. Krauss, 1989: Generation and Propagation of Annual Rossby Waves in the North Atlantic. *J. Phys. Oceanogr.*, **19**, 727–744.

Hirschi, J., J. Baehr, J. Marotzke, J. Stark, S. Cunningham, and J.-O. Beismann, 2003: A monitoring design for the Atlantic meridional overturning circulation. *Geophys. Res. Lett.*, **30**, 1413, doi:10.1029/2002GL016776.

Hirschi J. J.-M., J. Marotzke, 2007: Reconstructing the meridional overturning circulation from boundary densities and the zonal wind stress. *J. Phys. Oceanogr.,* **37**, 3, 743-763.

Hirschi J. J.-M., P.D. Killworth, J.R. Blundell, 2007: Subannual, seasonal and interannual

variability of the North Atlantic meridional overturning circulation. *J. Phys. Oceanogr.*, **37**, 5, 1246-1265.

Hirschi, J.J.M., P.D. Killworth, J.R. Blundell, and D. Cromwell, 2009: Sea Surface Height Signals as Indicators for Oceanic Meridional Mass Transports. *J. Phys. Oceanogr.*, **39**, 581–601.

IPCC, Climate Change 2007: The Scientific Basis: Contribution of Working Group I to the Fourth Assessment Report of the Intergovernmental Panel of Climate Change (Cambridge Univ. Press, New York, 2007).

Jayne, S. R., and J. Marotzke, 2001: The dynamics of ocean heat transport variability. *Rev. Geophys.*, **39**, 385-411.

Johns, W. E., et al., 2005: Estimating ocean transports with dynamic height moorings: An application in the Atlantic Deep Western Boundary Current. *Deep-Sea Res. I*, **52**, 1542-1567.

Johns, W.E., L.M. Beal, M.O. Baringer, J.R. Molina, S.A. Cunningham, T. Kanzow, and D. Rayner: 2008: Variability of Shallow and Deep Western Boundary Currents off the Bahamas during 2004–05: Results from the 26°N RAPID–MOC Array. *J. Phys. Oceanogr.*, **38**, 605–623.

Johns, W., L. Beal, M. Baringer, S. Cunningham, T. Kanzow, H. Bryden, J. Hirschi, J. Marotzke, C. Meinen, B. Shaw, and R. Curry: 2010: Continuous, array-based estimates of

Atlantic Ocean Heat transport at 26.5°N. (in preparation).

Johnson GC, Gruber N, 2007: Decadal water mass variations along 20 degrees W in the Northeastern Atlantic Ocean. Progr. Oceanogr., 73, 277-295, 2007.

Joyce, T.M., and P. Robbins, 1996: The Long-Term Hydrographic Record at Bermuda. *J. Climate*, **9**, 3121–3131.

Joyce, Terrence M., Robert S. Pickart, and Robert C. Millard, 1999: Long-term hydrographic changes at 52 and 66 W in the North Atlantic subtropical gyre and Caribbean. *Deep-Sea Research II*, **46**, 245̃278.

Kalnay, E., M. Kanamitsu, R. Kistler, W. Collins, D. Deaven, L. Gandin, et al., 1996: The NCEP/NCAR reanalysis project. *Bull. Am. Meteorol. Soc.,* **77**, 437–471. doi:10.1175/1520-0477.

Kanzow, T., 2000. Integrale Erfassung langperiodischer Transporte: Simulation und Optimierung eines verankerten Systems. *Diplom Thesis,* Christian-Albrechts-University, Kiel, 95 p.

Kanzow, T., Send, U., Zenk, W., Chave, A.D., Rhein, M., 2006: Monitoring the integrated deep meridional flow in the tropical North Atlantic: Lon-term performance of a geostrophic array. *Deep-Sea Res. I*, **53**, 528-546.

Kanzow, T., S. A. Cunningham, D. Rayner, J. J.-M. Hirschi, W. E. Johns, M. O. Baringer, H. L. Bryden, L. M. Beal, C. S. Meinen, and J. Marotzke, 2007: Flow compensation associated with the MOC at 26.5°N in the Atlantic. *Science*, **317,** 938-941.

Kanzow, T., J. J-M Hirschi, C. Meinen, D. Rayner, S. A Cunningham, J. Marotzke, W. E. Johns, H. L. Bryden, L. M. Beal, M. O. Baringer, 2008a: A prototype system for observing the Atlantic Meridional Overturning Circulation - scientific basis, measurement and risk mitigation strategies, and first results. *J. Operat. Oceanogr.*, **1**, 19 – 28.

Kanzow, T., U. Send, M. McCartney, 2008b: On the variability of the deep meridional transports in the tropical North Atlantic. *Deep-Sea Res. I*, **55**, 1601-1623, doi: 10.1016/j.dsr.2008.07.011

Kanzow, T, H. Johnson, D. Marshall, S.A. Cunningham, J. J-M. Hirschi, A. Mujahid, H.L. Bryden, and W.E. Johns, 2009: Basin-wide integrated volume transports in an eddy-filled ocean. *J. Phys. Oceanogr.,* 39 (12), 3091–3110, DOI: 10.1175/2009JPO4185.1 .

Kanzow, T., and M. Visbeck, 2009: Ocean Currents as indicator of climate change. In: *Climate Change: Observed Impacts on Planet Earth.* Letcher, T. (Editor), Elsevier. .

Kieke, Dagmar, Birgit Klein, Lothar Stramma, Monika Rhein, and Klaus Peter Koltermann (2009), Variability and propagation of Labrador Sea Water in the southern subpolar North Atlantic. *Deep-Sea Res. I.*, 56(10), 1656-1674.

Killworth, P.D, and J.R. Blundell, 2005: The dispersion relation for planetary waves in the presence of mean flow and topography. Part II: Twodimensional examples and global results. *J. Phys. Oceanogr.*, 35, 2110–213.

Köhl, A.. 2005: Anomalies of meridional overturning: Mechanisms in the North Atlantic. *J. Phys. Oceanogr.*, **35**, 1455-1472.

Larsen, J. C., 1992: Transport and heat flux of the Florida Current at 27°N derived from cross-stream voltages and profiling data: theory and observations, *Phil. Trans. Roy. Soc. London*, **A 338**, 169-236.

Latif, M., E. Roeckner, M. Botzet, M. Esch, H. Haak, S. Hagemann, J. Jungclaus, S. Legutke, S. Marsland, U. Mikolajewicz, and J. Mitchell, 2004: Reconstructing, Monitoring, and Predicting Multidecadal-Scale Changes in the North Atlantic Thermohaline Circulation with Sea Surface Temperature. *J. Clim.*, **17**, 1605-1614.

Lee T.N., W.E. Johns, R.J. Zantopp and E.R. Fillenbaum, 1996: Moored observations of western boundary current variability and thermocline circulation at 26.5°N in the subtropical North Atlantic. *J. Phys. Oceanogr.,* **26** (6), 962-983.

Lee, T., 2009: Consistency of AMOC estimates from global ocean data assimilation (ODA) products. US AMOC annual meeting. 4-6 May, 2009, Abstract: www.atlanticmoc.org/AMOC2009agenda.php

Levitus, S., 1982: Climatological Atlas of the World Ocean, *NOAA Professional Paper*, **13**,

191pp.

Longworth, H.R., 2007: Constraining variability of the Atlantic meridional overturning circulation at 26.5N from historical observations. Ph.D. Thesis, School of Ocean and Earth Science, University of Southampton. Southampton. United Kingdom. 198p.

Lumpkin, R., et al., 2007: Global Ocean Meridional Overturning. *J. Phys. Oceanog.*, **38**, DOI: 10.1175/2007JPO3636.1171.

McCartney, M.S., and R. Curry, 1993: Trans-equatorial flow of Antarctic bottom water in the Western Atlantic Ocean. *J. Phys. Oceanogr.*, **23**, 1264–1276.

Mercier, H. and K. Speer, 1998: Transport of bottom water in the Romanche Fracture Zone and Chain Fracture Zone. *J. Phys. Oceanogr.*, **28**, 779-790.

Meinen, C. S., M. O. Baringer, and R. F. Garcia, 2010: Florida Current Transport Variabilty: An Analysis of Annual and Longer-Period Signals. *Deep-Sea. Res. I*, doi: 10.1016/j.dsr.2010.04.001 (in press).

Orsi, A.H., W.M. Smethie, and J.L. Bullister, 2002: On the total input of Antarctic waters to the deep ocean: A preliminary estimate from chlorofluorocarbon measurements. *J. Geophys. Res.*, **107** (C8), 3122, doi:10.1029/2001JC000976.

Osychny, V., and P. Cornillon, 2004: Properties of Rossby Waves in the North Atlantic Estimated from Satellite Data. *J. Phys. Oceanogr.*, **34**, 61–76.

Risien, C.M., and D.B. Chelton, 2008: A Global Climatology of Surface Wind and Wind Stress Fields from Eight Years of QuikSCAT Scatterometer Data. *J. Phys. Oceanogr.*, **38**, 2379–2413.

Roemmich, D. and C. Wunsch, 1985: Two transatlantic sections: Meridional ciculation and heat flux in the subtropical North Atlantic Ocean, Deep Sea-Res.**32**, 619

Schlax, M.G., D.B. Chelton, and M.H. Freilich, 2001: Sampling Errors in Wind Fields Constructed from Single and Tandem Scatterometer Datasets. *J. Atmos. Oceanic Technol.*, **18**, 1014–1036.

Schott, F. A., J. Fischer, M. Dengler, and R. Zantopp (2006), Variability of the Deep Western Boundary Current east of the Grand Banks, *Geophys. Res. Lett.*, **33**, L21S07, doi:10.1029/2006GL026563.

Smith, G.C, K. Haines, T. Kanzow, and S. Cunningham, 2009: Impact of hydrographic data assimilation on the Atlantic meridional overturning circulation. *Ocean Sci. Discuss.*, 6, 2667-2715. (manuscript under review: http://www.ocean-sci-discuss.net/6/2667/2009/)

Sturges, W., B.G. Hong, and A.J. Clarke, 1998: Decadal Wind Forcing of the North Atlantic Subtropical Gyre. *J. Phys. Oceanogr.*, **28**, 659–668.

Talley, L. D., et al., 2003: Data-based Meridional Overturning Streamfunctions for the Global Ocean. *J. Clim.*, **16**, DOI: 10.1175/2787.1171.

Tennekes, H. and J. L. Lumley, 1972: A first course in turbulence. *The MIT Press*, 300 pp.

Wijffels, S. E., 2001: Ocean transport of fresh water. *Ocean Circulation & Climate: Observing and Modelling the Global Ocean*, G. Siedler, J. Church, and J. Gould, Eds., Academic Press, 715.

Woodgate, R. A. and K. Aagaard, 2005: Revising the Bering Strait freshwater flux into the Arctic Ocean. *Geophys. Res. Lett.*, **32,** doi:10.1029/2004/GL021747.

Wunsch, C. and P. Heimbach, 2009: The globally integrated ocean circulation (MOC), 1992-2006: seasonal and decadal variability, *J. Phys. Oceangr.*, 39, 351-368.

List of Figure Captions

Fig. 1: Atlantic Meridional Overturning stream function $\Psi(y,z)$ from observations (from Talley et al., 2003), with a 2 Sv contour interval. The observations reveal two interhemispheric overturning cells, with the deep one involving Antarctic Bottom Water and the shallower one North Atlantic Deep Water.

Fig. 2: Upper panel: The distribution of moorings along 26.5°N in the subtropical North Atlantic. Lower panel: Section of density (and bottom pressure) moorings along 26.5°N. The current meter moorings west of WB2 are not shown here for clarity (see Fig. 3).

Fig. 3: Moorings near the western boundary (off Abaco, the Bahamas). Density sensors, bottom pressure recorders and current meters are denoted as crosses, squares and circles, respectively. The dots at WBA and WB0 indicate the part of the water column covered by Acoustic Doppler Current Profiler (ADCP) measurements. WBH1 and WBH2 were only deployed during the period 04/2004 to 04/2005.

Fig. 4: Zonally integrated northward transport [Sv m^{-1}] across 26.5°N shallower than 1000 m (upper panel) and deeper than 600 m (lower panel). The bold, solid line represents the April 2004 to April 2008 time mean of $T_{AMOC}(z)$, the dashed line is the time mean of $T_{MO}(z)$. The abyssal transport structure (below the gray line) is estimated based on the synthetic approximation to historical estimates from Fig. A1.

Fig. 5: Overturning streamfunction $\Psi(z) = \int_z^0 T_{AMOC}(z)\,\mathrm{d}z$ at 26.5N, based on 10-day low-pass filtered $T_{AMOC}(z)$. One profile every five days has been plotted over the 48-month-long

measurement period between April 2004 and April 2008. The red dots on each profile mark the maximum northward transport Ψ^{MAX} and the corresponding depth h_c.

Fig. 6: Mid-ocean transport, $T_{MO}(z)$, shallower than 1200 m (panel A) and deeper than 600 m (panel B) in Sv m^{-1} (note that the two panel overlap in the 600 – 1200 m depth range) . The data are 10-day low-pass filtered. Note that the transport scale in panel A is much broader than in B. The interface depth between the upper and lower branches of the upper (NADW) overturning cell h_{ZC} is given as white dotted line.

Fig. 7: The thin lines denote the time series of Ψ^{MAX} (red), T_{GS} (blue), T_{EK} (black) and T_{UMO} (magenta) for the period between April 2004 and April 2008. The data have been 10-day low-pass filtered. Also shown is the contribution of the compensation transport to Ψ^{MAX} (i.e., $T_C(z)$ integrated between the sea surface and the level of no motion). The bold lines represent the best estimates of the long-term seasonal cycles of each transport component (see section 3c and Fig. 10).

Fig. 8: Solid lines denote power spectra of Ψ^{MAX} (red), T_{GS} (blue), T_{EK} (black) and T_{UMO} (magenta) for the period from April 2004 to April 2008 (as shown in Fig. 7). Also shown for reference purposes as dashed lines are transport spectra of T_{GS} (blue) and T_{EK} (black) based on time series between March 1982 and January 2008. The long T_{EK} time series is based on NCEP/NCAR re-analysis data (Kalnay, 1996The spectra are based on Welch's periodogram method using a 365 (730)-days-wide Hamming window and 182 (365) days overlap between consecutive data segments for periods ≤ (>) 365 days.

Fig. 9: 10-day low pass filtered time series of the western (Ψ_{MOW}^{MAX}, black line) and eastern

(Ψ_{MOE}^{MAX}, gray line) boundary contributions of the mid-ocean section to the overturning strength (see section 2.3 for details). For the computation T_{GS} and T_{EK} have been prescribed as time-invariant.

Fig. 10: Seasonal cycles (black solid lines) of T_{GS} (A), T_{EK} (B), T_{UMO}(C) and Ψ^{MAX} (D), as obtained from month-wise averages of the time series between April 2004 and April 2008. The gray envelopes represent the standard error of each month (as obtained from the 4 realisations of monthly averages that are available for each month). The dashed lines in the panels A and B represent seasonal cycles of T_{GS} and T_{EK} based on the 26 year long time series (10/1982-01/2008) used for the computation of the spectra in Fig. 8. The dashed line in panel D represents the best guess of the long-term seasonal cycle of Ψ^{MAX} (see text). Positive values denote northward flow.

Fig. 11: Monthly mean mid-ocean transport profile [Sv m^{-1}] for the period April 2004 to April 2008, after removal of the annual mean and the barotropic (vertical mean) flow for each month.

Fig. 12: Seasonal cycles of the western (left) and eastern (right) boundary contributions to the mid-ocean section of the overturning strength (Ψ_{MOW}^{MAX}, Ψ_{MOE}^{MAX}) based on the time series shown in Fig. 9. The gray envelope represents the standard error as in Fig. 10. Positive values correspond to northward flow. The sum of the seasonal anomalies of Ψ_{MOW}^{MAX} and Ψ_{MOE}^{MAX} therefore corresponds to the seasonal anomalies of T_{UMO}.

Fig. 13: Seasonal wind stress curl anomaly [10^7 N m^{-3}] along 26.5°N relative to annual mean value (panel A) based on SCOW climatology (Risien and Chelton, 2009). This field is used to force the mid-ocean response analysis illustrated in Fig. 14. Panel B: Wind stress curl anomaly extracted at 26.5°N / 16.1°W from the data shown panel A. The wind stress curl variability is largest near the eastern boundary, where strong seasonal variations in southward winds along the African coast (maximum in boreal summer) produce a large seasonal cycle.

Fig. 14: The mid-ocean response from the forced Rossby wave model (eqn. 8-10), using the SCOW seasonal wind stress curl anomaly climatology (Fig. 13), summed over the first two baroclinic modes. Panel A shows the resulting anomaly of the mid-ocean transport profile, $T_{MO}^{\nabla\times\tau}(z)$, and panel B shows the associated mid-ocean AMOC anomaly, Ψ_{MO}^{MAX}, calculated as the transport anomaly in the upper ocean above the zero level (~950 m) of the $T_{MO}^{\nabla\times\tau}(z)$. The curves in panel B show the total AMOC anomaly (blue), and the contributions resulting from the variability forced at the eastern boundary (green) and at the western boundary (red).

Fig. 15: Monthly anomalies of the wind stress curl [10^7 N m^{-3}] at 27.25°N / 14.50°W near the eastern boundary density moorings EBH4 and EBH5. Each thin line represents one year of monthly averaged data between 1999 and 2009. The bold lines represent seasonal cycles (dashed of the 2004 – 2008 average and solid for the 1999 – 2009 average). Data source: 0.25° x 0.25° gridded Quickscat scatterometer wind stress from Jet Propulsion Laboratory (http://podaac.jpl.nasa.gov/DATA_CATALOG/quikscatinfo.html).

Fig. 16: Ψ^{MAX} inferred from five hydrographic snapshot estimates between 1957 and 2004

(solid diamonds), as reproduced from Bryden et al (2005). The hydrography cruises were carried out in different seasons, namely in October 1957, August / September 1982, July / August 1991, February 1998 and April 2004. The open squares represent the historical estimates of Ψ^{MAX} with seasonal anomalies of T_{UMO} (Fig. 10c; Table 2) subtracted.

Fig. A1: Abyssal, zonally integrated transport across 26.5°N from hydrographic cruises in 1957, 1981, 1992, 1998, 2004 (as presented by Bryden et al., 2005). The synthetic approximation of the transports below 5000 m (black line) represents the transport shear profile used in this study to extend the AMOC transport profile $T_{AMOC}(z)$ into the AABW range.

Illustrations and tables

Table 1: Basic statistics of the different transport components [Sv] discussed in this study for the period between 04/2004 and 04/2008 (the values in brackets in columns 2 and 4 refer to the period between 10/1982 and 01/2008) based on 10-day low-pass filtered data. SD and SE denote standard deviation and standard error, respectively. The standard error (SE) in column 4 represents the average of the 12 monthly standard errors. The integral time scale of the four-year-long time series in column 4 have been computed according to Appendix B. *Calculations based on (7).

Component	Mean / SD 04/04-10/07 (10/82-01/08)	Integral time scale [days] / degrees of freedom	Seasonal cycle: Min[mm] / Max[mm] / SE 04/2004 - 04/2008 (10/1982 - 01/2008)
T_{GS}	31.7 / 2.9 (32.1 / 3.1)	29 / 51	30.5 [Nov] / 33.4 [Jul] / 1.1 (30.6 [Jan] / 33.6 [Jul])
T_{EK}	3.5 / 3.5 3.7 /3.1	12 / 121	1.5 [Mar] / 5.6 [Dec] / 0.8 (3.0 [Jun] / 5.1 [Jan])
T_{UMO}	-16.5 / 3.2 (n/a)	47 / 32	-19.3 [Apr]/-13.4 [Nov]/0.9 (n/a)
Ψ^{MAX}	18.7 / 4.8 (n/a)	46 / 32	14.0 [Mar] / 21.8 [Jul] / 1.4 (14.8 [Mar] / 21.5 [Jul])*
Ψ_{W}^{MAX}	18.7 / 3.0 (n/a)	40 / 37	17.6 [Feb] / 21.2 [Aug] /1.2 (n/a)
Ψ_{MOW}^{MAX}	18.7 / 2.3 (n/a)	34 / 43	16.9 [Feb] / 20.8 [Aug] /0.9 (n/a)
Ψ_{MOE}^{MAX}	18.7 / 2.1 (n/a)	43 /34	16.6 [Apr] / 22.0 [Oct] / 0.5 (n/a)

Table 2: Seasonal bias correction of the Bryden at al. (2005a) historical estimates of ψ^{MAX} (see Fig. 16). Corrections have only been applied to the upper mid-ocean transport (T_{UMO}), as Bryden et al. (2005) used constant values for T_{EK} and T_{GS} (see text). Column 1, 2, 3 and 4 give the cruise dates, the historical estimates of ψ^{MAX} (solid line in Fig. 16), the seasonal anomalies of T_{UMO} (from Fig. 10c) corresponding to the months in which the measurements cruises were conducted, and the seasonal-anomaly-corrected estimates of ψ^{MAX} (dashed line in Fig. 16), respectively.

Cruise	ψ^{MAX} [Sv] (Bryden et. al)	T_{UMO} seasonal anomaly [Sv]	ψ^{MAX} [Sv] with seasonal anomaly removed
Oct. 1957	22.9	2.8	20.1
Aug. / Sep. 1981	18.7	1.4	17.3
Jul. / Aug. 1992	19.4	0.9	18.5
Feb. 1998	16.1	-2.0	18.1
Apr. 2004	14.8	-2.7	17.5

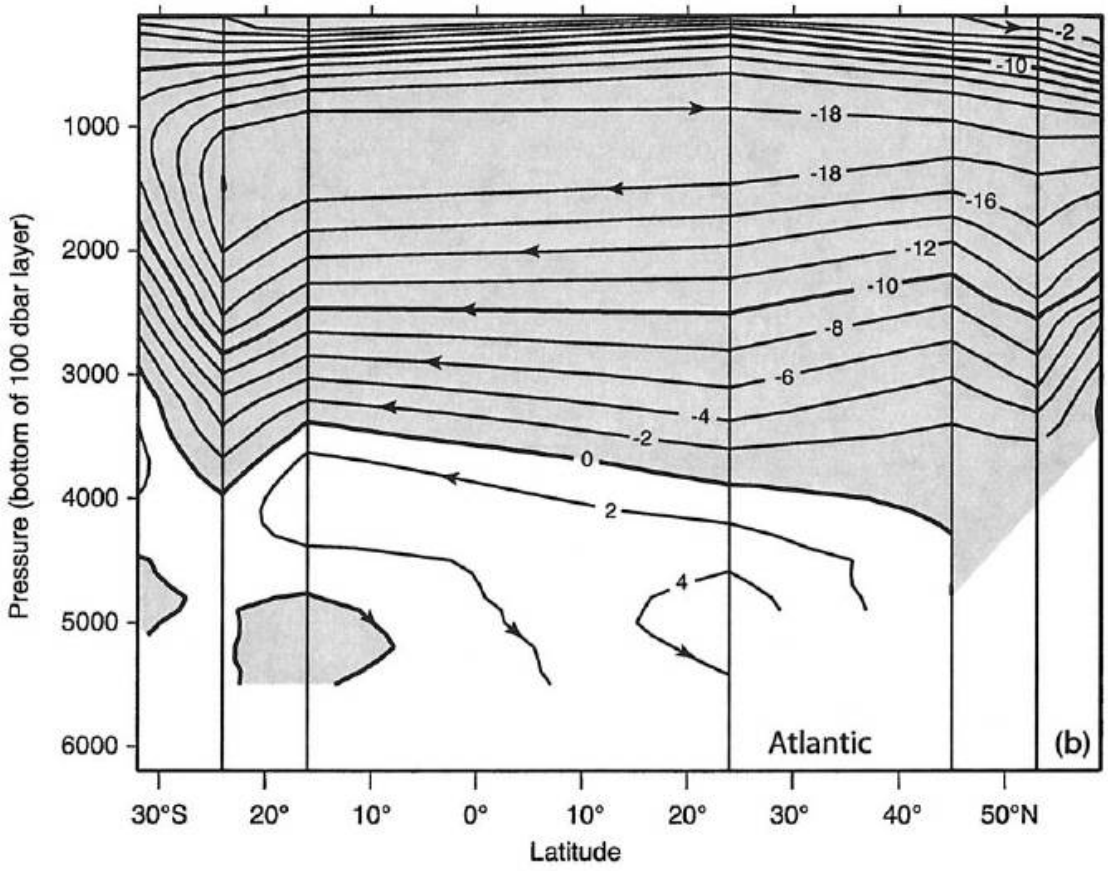

1225

Fig. 1: Atlantic Meridional Overturning stream function $\Psi(y,z)$ from observations (from Talley et al., 2003), with a 2 Sv contour interval. The observations reveal two interhemispheric overturning cells, with the deep one involving Antarctic Bottom Water and
1230 the shallower one involving North Atlantic Deep Water.

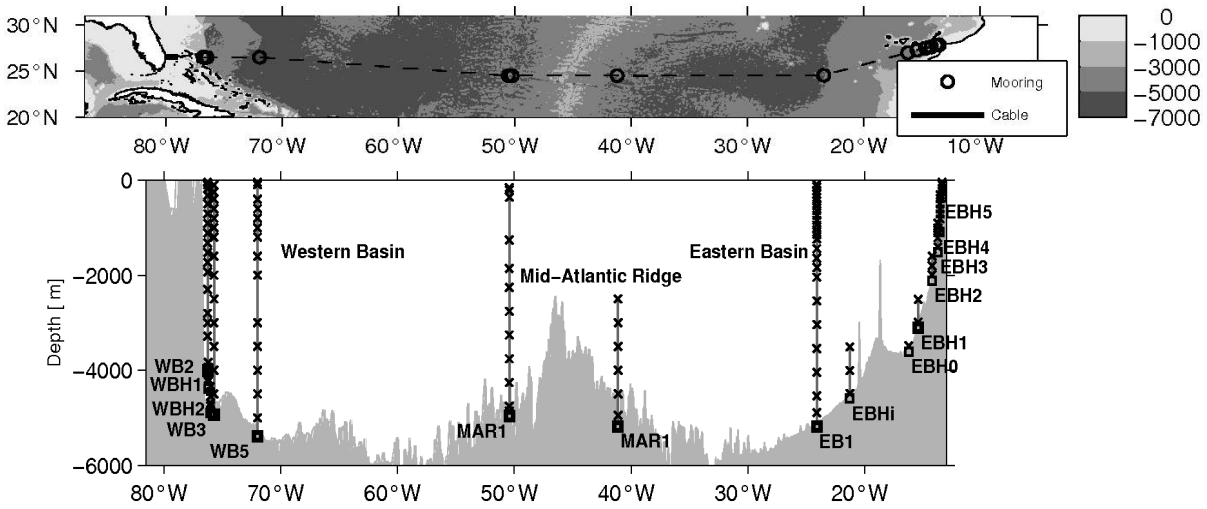

Fig. 2: Upper panel: The distribution of moorings along 26.5°N in the subtropical North Atlantic. Lower panel: Section of density (and bottom pressure) moorings along 26.5°N. The current meter moorings west of WB2 are not shown here for clarity (see Fig. 3).

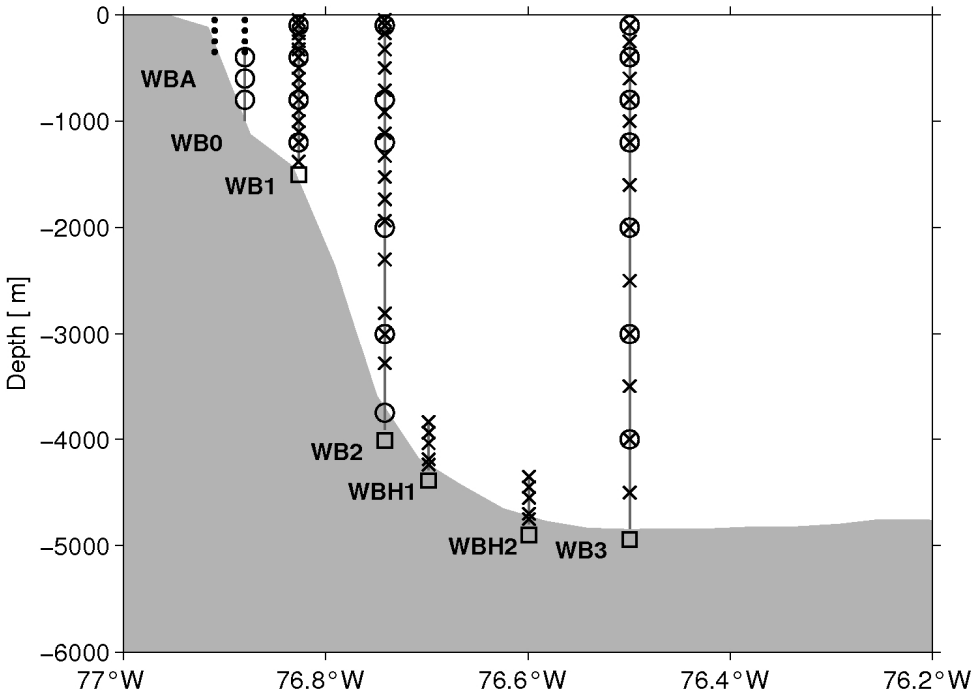

Fig. 3: Moorings near the western boundary (off Abaco, the Bahamas). Density sensors, bottom pressure recorders and current meters are denoted as crosses, squares and circles, respectively. The dots at WBA and WB0 indicate the part of the water column covered by Acoustic Doppler Current Profiler (ADCP) measurements. WBH1 and WBH2 were only deployed during the period 04/2004 to 04/2005.

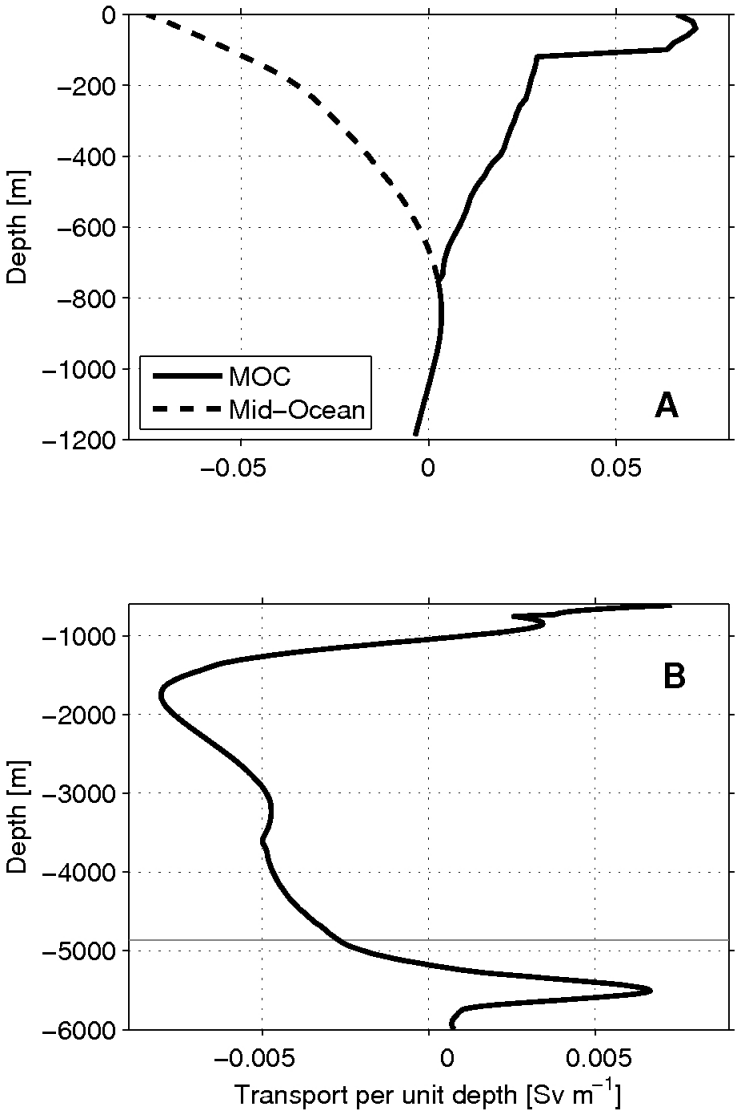

Fig. 4: Zonally integrated northward transport [Sv m^{-1}] across 26.5°N shallower than 1000 m (upper panel) and deeper than 600 m (lower panel). The bold, solid line represents the April 2004 to April 2008 time mean of $T_{AMOC}(z)$, the dashed line is the time mean of $T_{MO}(z)$. The abyssal transport structure (below the gray line) is estimated based on the synthetic approximation to historical estimates from Fig. A1.

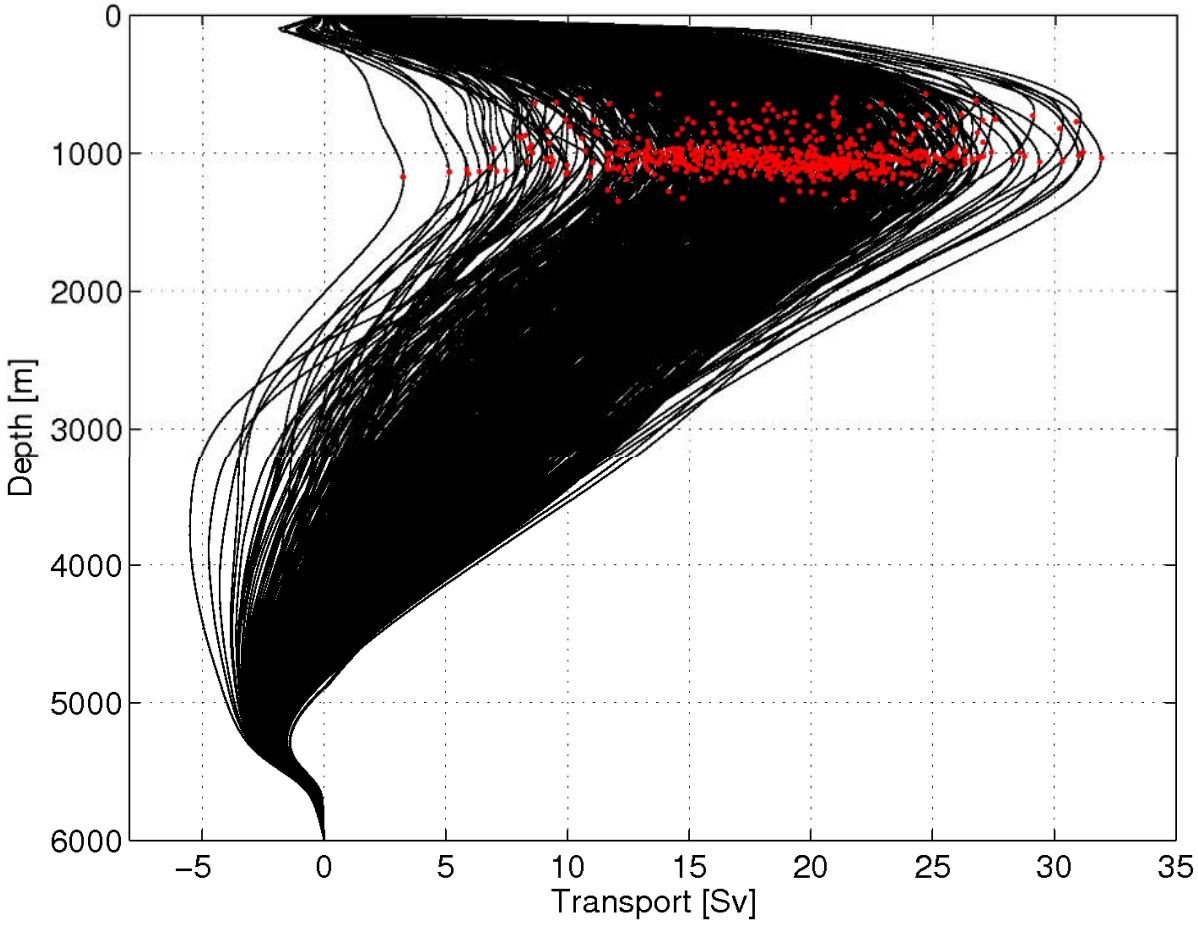

Fig. 5: Overturning streamfunction $\Psi(z) = \int_{z}^{0} T_{AMOC}(z)\,\mathrm{d}z$ at 26.5N, based on 10-day low-pass filtered $T_{AMOC}(z)$. One profile every five days has been plotted over the 48-month-long measurement period between April 2004 and April 2008. The red dots on each profile mark the maximum northward transport Ψ^{MAX} and the corresponding depth h_{ZC}.

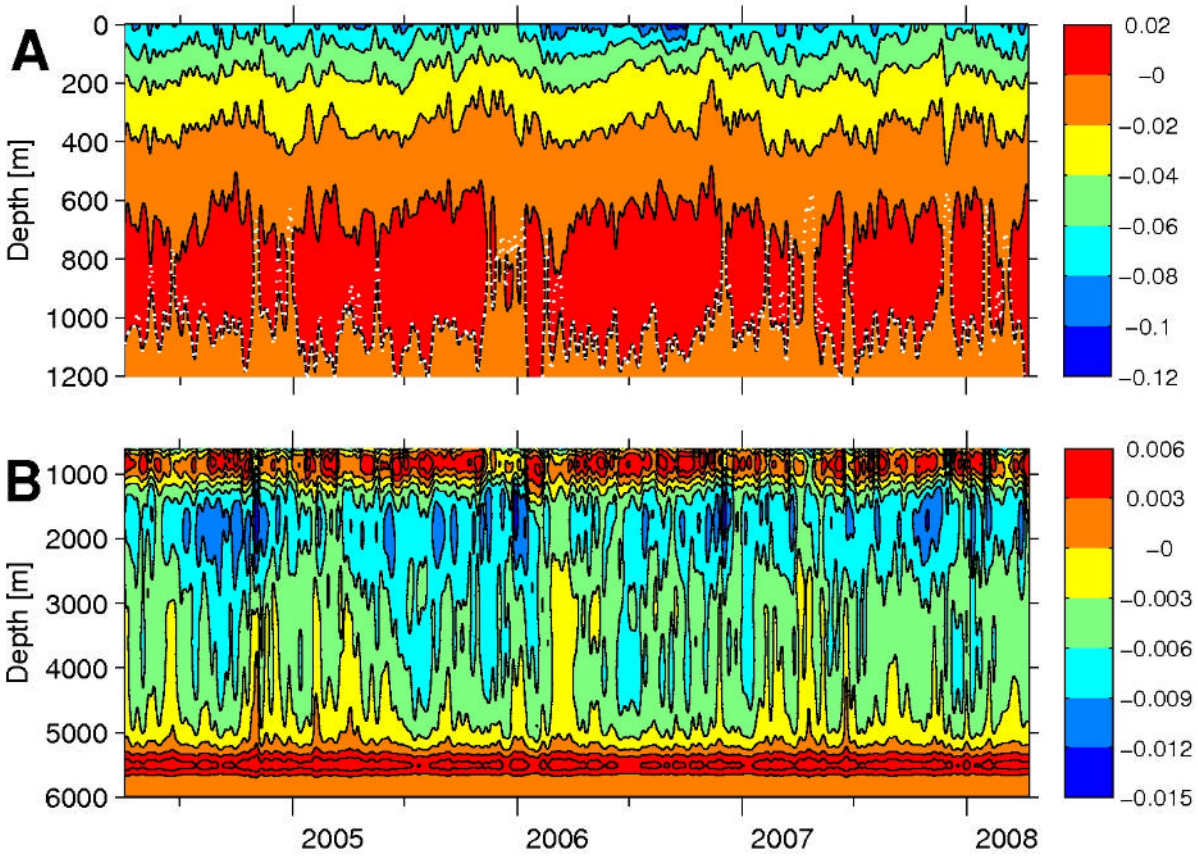

Fig. 6: Mid-ocean transport, $T_{MO}(z)$, shallower than 1200 m (panel A) and deeper than 600 m (panel B) in Sv m^{-1} (note that the two panel overlap in the 600 – 1200 m depth range) . The data are 10-day low-pass filtered. Note that the transport scale in panel A is much broader than in B. The interface depth between the upper and lower branches of the upper (NADW) overturning cell h_{ZC} is given as white dotted line.

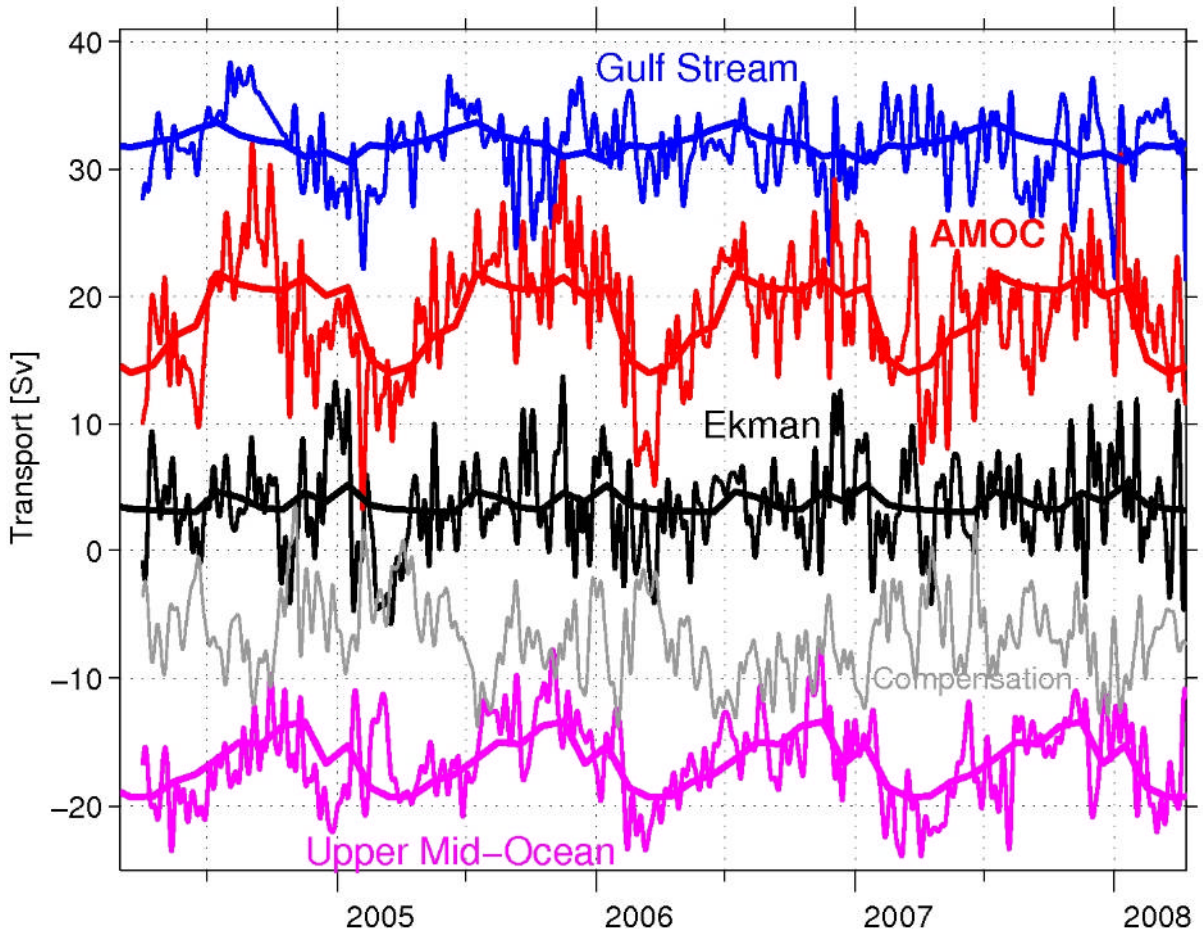

Fig. 7: The thin lines denote time series of Ψ^{MAX} (red), T_{GS} (blue), T_{EK} (black) and T_{UMO} (magenta) for the period between April 2004 and April 2008. The data have been 10-day low-pass filtered. Also shown is the contribution of the compensation transport to Ψ^{MAX} (i.e., $T_C(z)$ integrated between the sea surface and the level of no motion). The bold lines represent the best estimates of the long-term seasonal cycles of each transport component (see section 3c and Fig. 10).

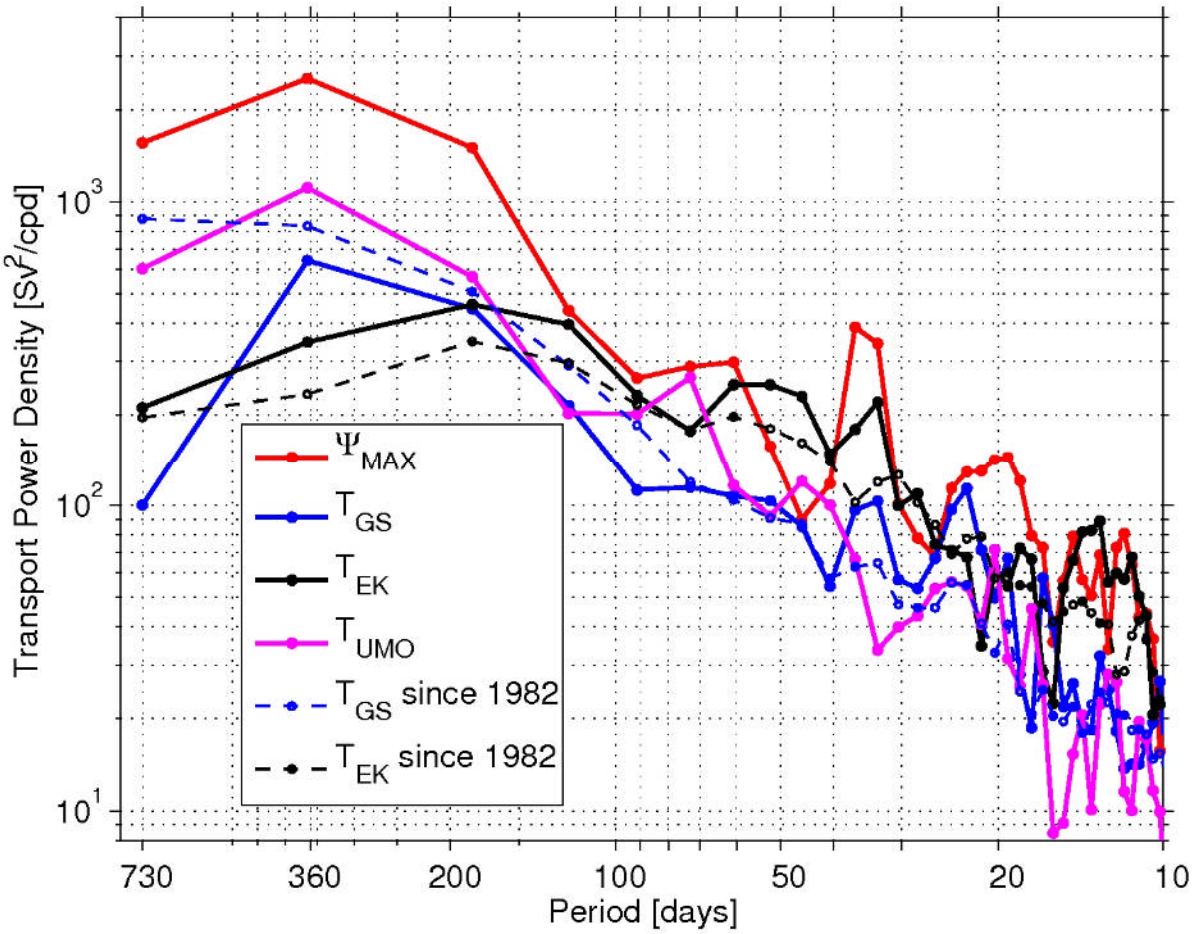

Fig. 8: Solid lines denote power spectra of Ψ^{MAX} (red), T_{GS} (blue), T_{EK} (black) and T_{UMO} (magenta) for the period from April 2004 to April 2008 (as shown in Fig. 7). Also shown for reference purposes as dashed lines are transport spectra of T_{GS} (blue) and T_{EK} (black) based on time series between March 1982 and January 2008. The long T_{EK} time series is based on NCEP/NCAR re-analysis data (Kalnay, 1996). The spectra are based on Welch's periodogram method using a 365 (730)-days-wide Hamming window and 182 (365) days overlap between consecutive data segments for periods ≤ (>) 365 days.

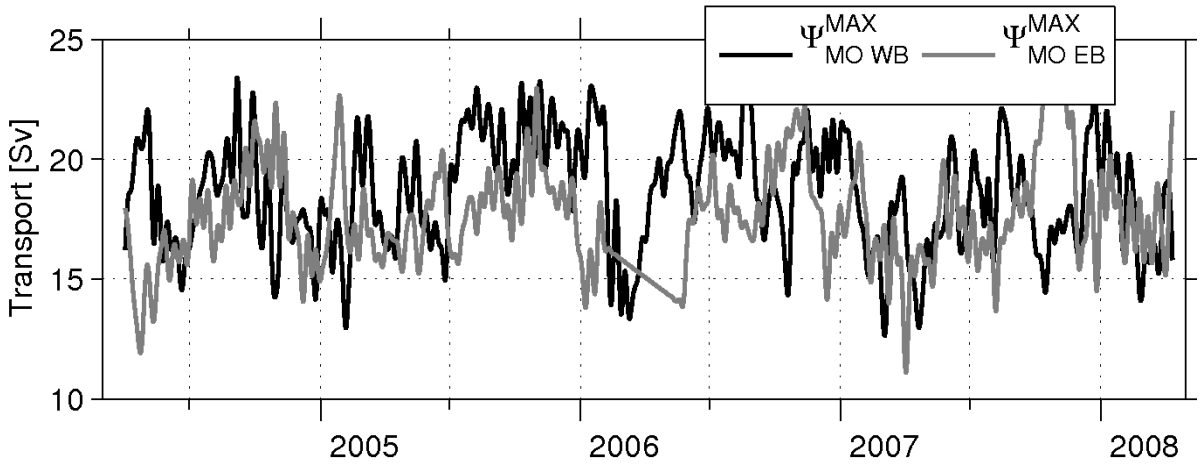

Fig. 9: 10-day low pass filtered time series of the western (Ψ_{MOW}^{MAX}, black line) and eastern (Ψ_{MOE}^{MAX}, gray line) boundary contributions of the mid-ocean section to the overturning strength (see section 2.3 for details). For the computation T_{GS} and T_{EK} have been prescribed as time-invariant.

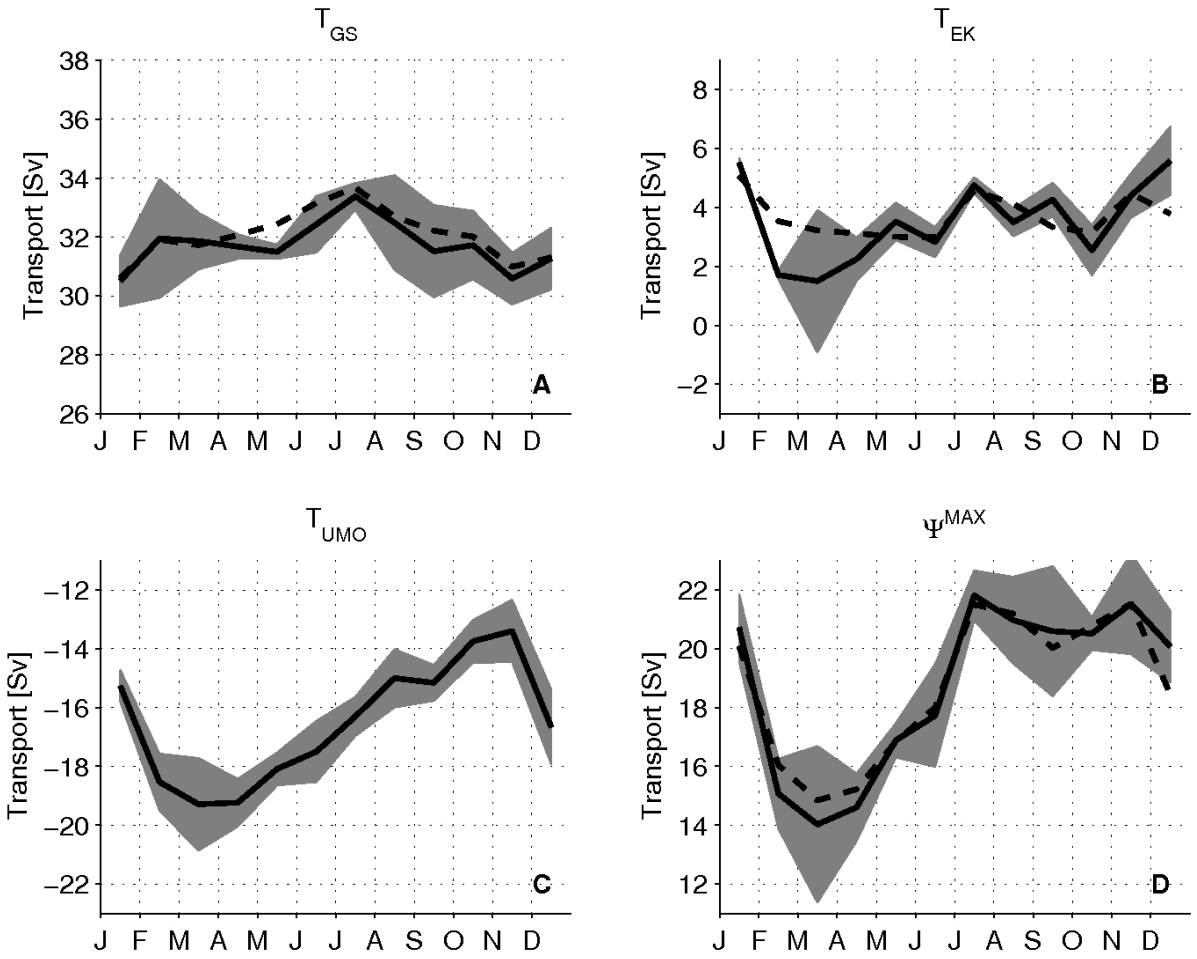

Fig. 10: Seasonal cycles (black solid lines) of T_{GS} (A), T_{EK} (B), T_{UMO}(C) and Ψ^{MAX} (D), as obtained from month-wise averages of the time series between April 2004 and April 2008. The gray envelopes represent the standard error of each month (as obtained from the 4 realisations of monthly averages that are available for each month). The dashed lines in the panels A and B represent seasonal cycles of T_{GS} and T_{EK} based on the 26 year long time series (10/1982-01/2008) used for the computation of the spectra in Fig. 8. The dashed line in panel D represents the best guess of the long-term seasonal cycle of Ψ^{MAX} (see text). Positive values denote northward flow.

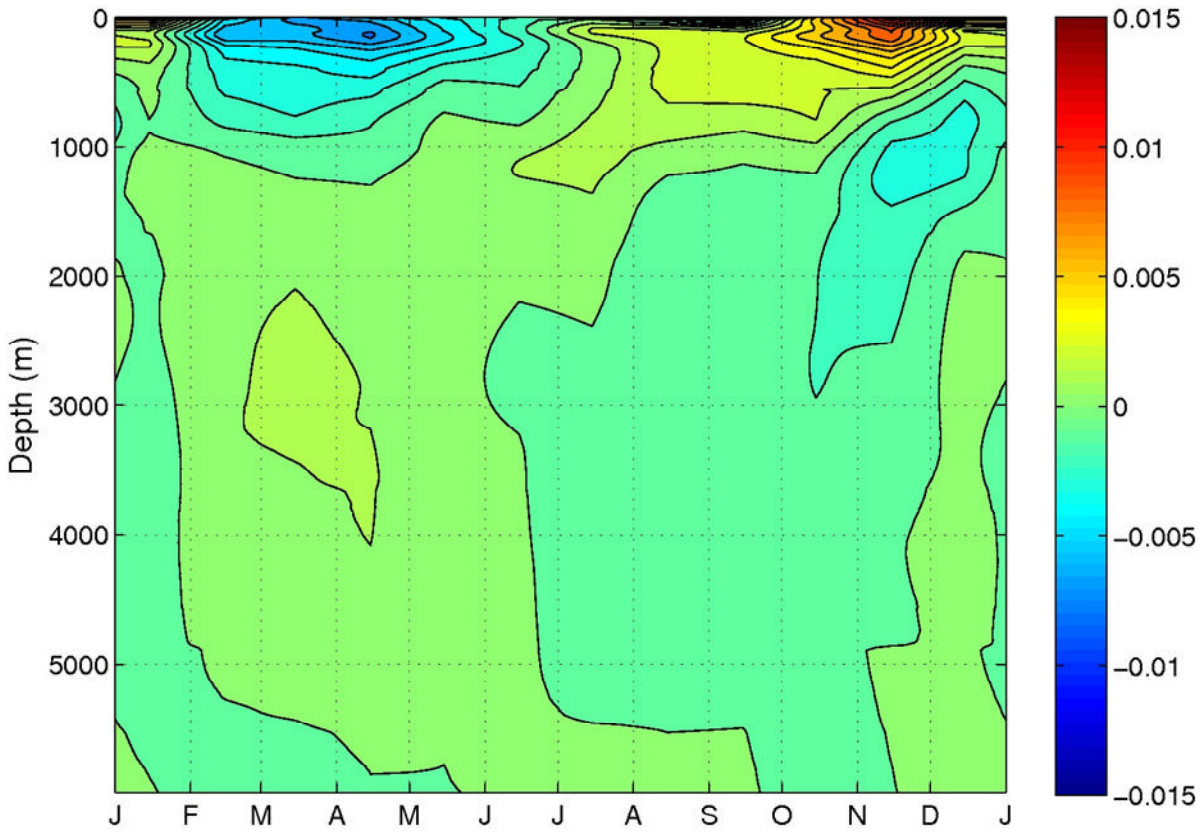

Fig. 11: Monthly mean mid-ocean transport profile [Sv m^{-1}] for the period April 2004 to April 2008, after removal of the annual mean and the barotropic (vertical mean) flow for each month.

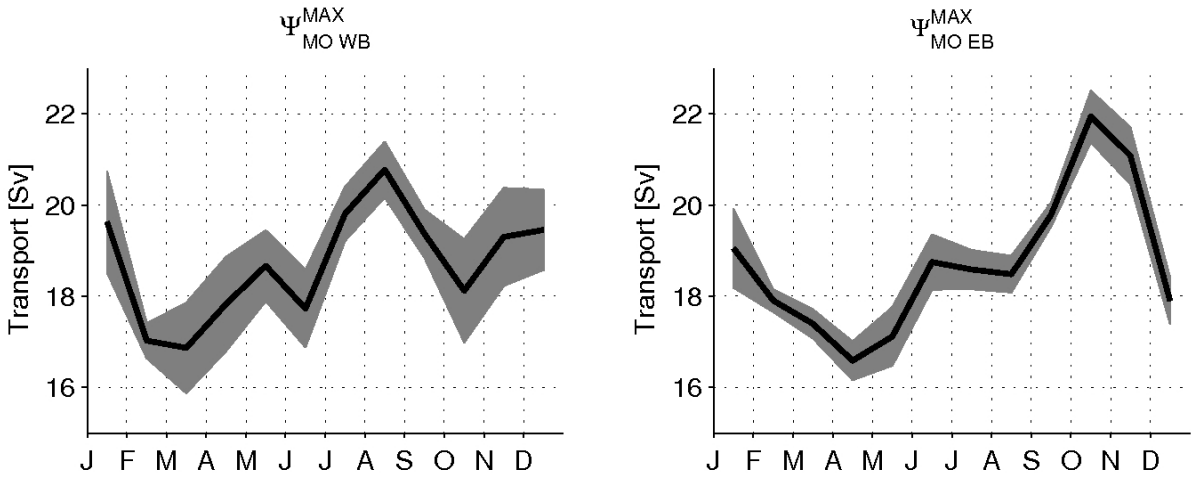

1380

Fig. 12: Seasonal cycles of the western (left) and eastern (right) boundary contributions to the mid-ocean section of the overturning strength (Ψ^{MAX}_{MOW}, Ψ^{MAX}_{MOE}) based on the time series shown in Fig. 9. The gray envelope represents the standard error as in Fig. 10. Positive values correspond to northward flow. The sum of the seasonal anomalies of Ψ^{MAX}_{MOW}

1385 and Ψ^{MAX}_{MOE} therefore corresponds to the seasonal anomalies of T_{UMO}.

1390

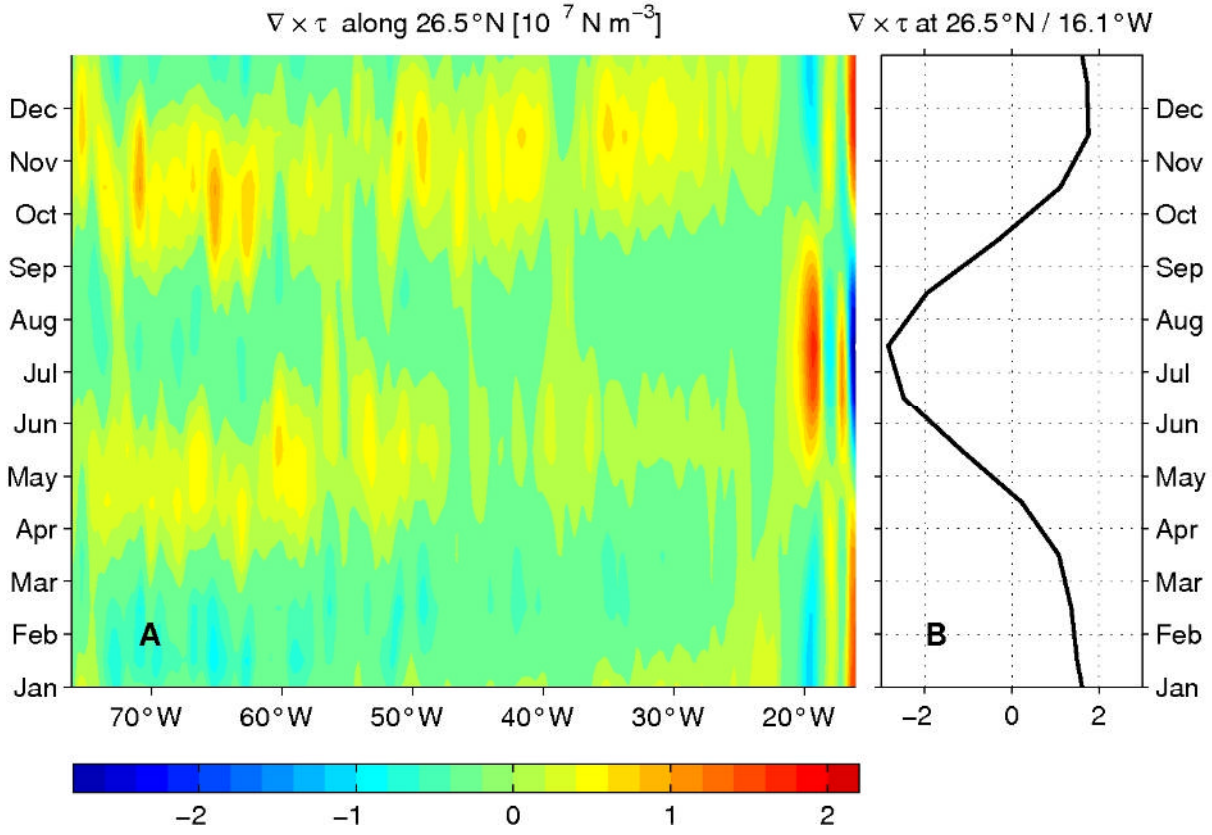

1395 Fig. 13: Seasonal wind stress curl anomaly [10^7 N m^{-3}] along 26.5°N relative to annual mean value (panel A) based on SCOW climatology (Risien and Chelton, 2009). This field is used to force the mid-ocean response analysis illustrated in Fig. 14. Panel B: Wind stress curl anomaly extracted at 26.5°N / 16.1°W from the data shown panel A. The wind stress curl variability is largest near the eastern boundary, where strong seasonal
1400 variations in southward winds along the African coast (maximum in boreal summer) produce a large seasonal cycle.

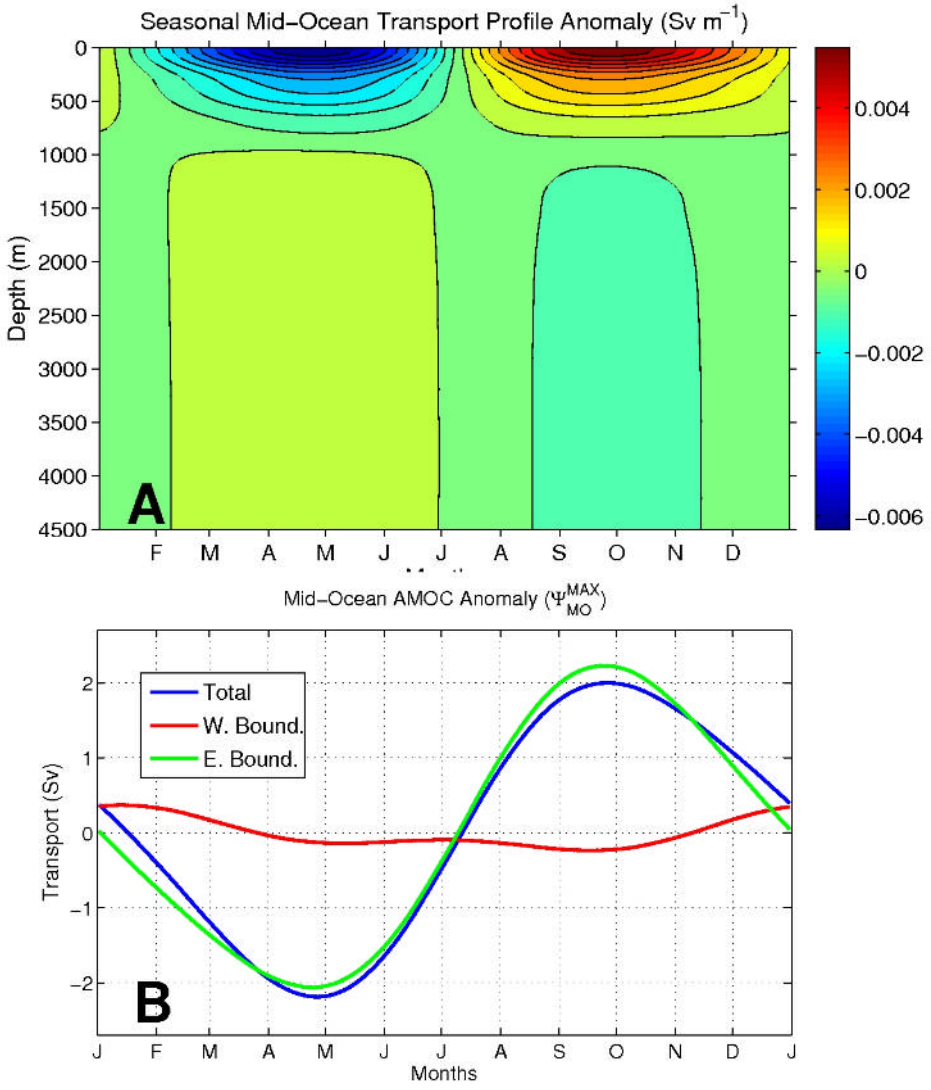

Fig. 14: The mid-ocean response from the forced Rossby wave model (eqn. 8-10), using the SCOW seasonal wind stress curl anomaly climatology (Fig. 13), summed over the first two baroclinic modes. Panel A shows the resulting anomaly of the mid-ocean transport profile, $T_{MO}^{\nabla\times\tau}(z)$, and panel B shows the associated mid-ocean AMOC anomaly, Ψ_{MO}^{MAX}, calculated as the transport anomaly in the upper ocean above the zero level (~950 m) of the $T_{MO}^{\nabla\times\tau}(z)$. The curves in panel B show the total AMOC anomaly (blue), and the contributions resulting from the variability forced at the eastern boundary (green) and at the western boundary (red).

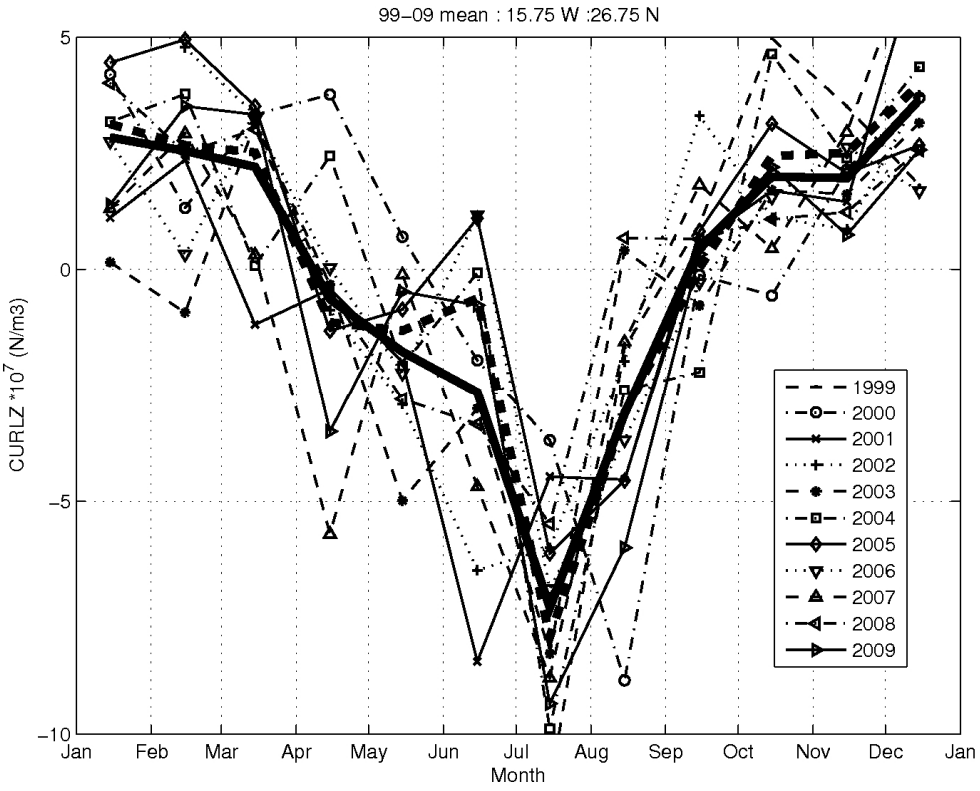

Fig. 15: Monthly anomalies of the wind stress curl [10^7 N m^{-3}] at 27.25°N / 14.50°W near the eastern boundary density moorings EBH4 and EBH5. Each thin line represents one year of monthly averaged data between 1999 and 2009. The bold lines represent seasonal cycles (dashed of the 2004 – 2008 average and solid for the 1999 – 2009 average). Data source: 0.25° x 0.25° gridded Quickscat scatterometer wind stress from Jet Propulsion Laboratory (http://podaac.jpl.nasa.gov/DATA_CATALOG/quikscatinfo.html).

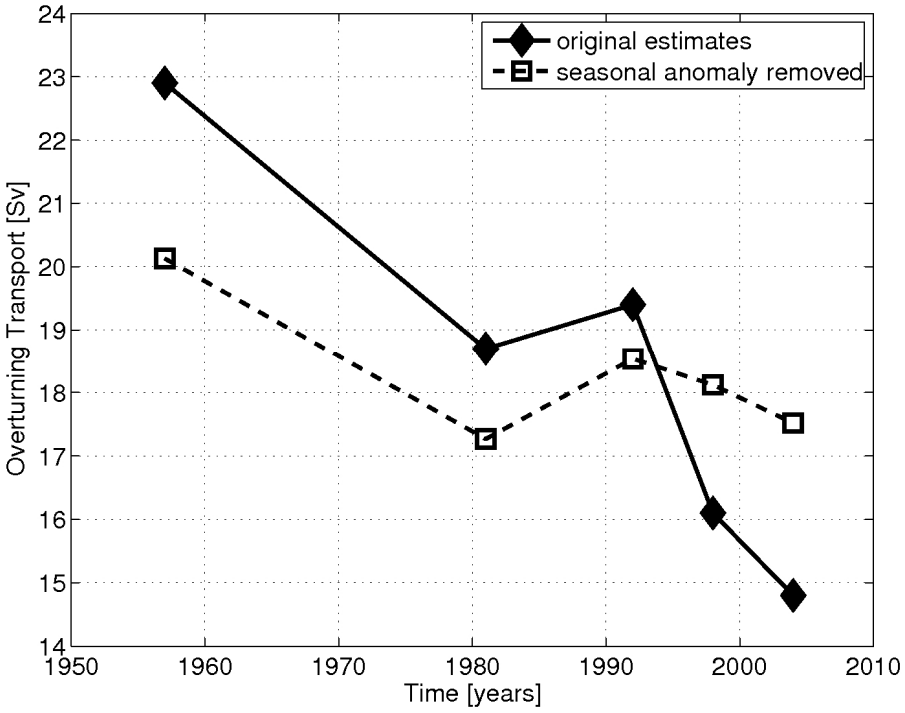

Fig. 16: Ψ^{MAX} inferred from five hydrographic snapshot estimates between 1957 and 2004 (solid diamonds), as reproduced from Bryden et al (2005a). The hydrography cruises were carried out in different seasons, namely in October 1957, August / September 1982, July / August 1991, February 1998 and April 2004. The open squares represent the historical estimates of Ψ^{MAX} with seasonal anomalies of T_{UMO} (Fig. 10c) subtracted (see Table 2).

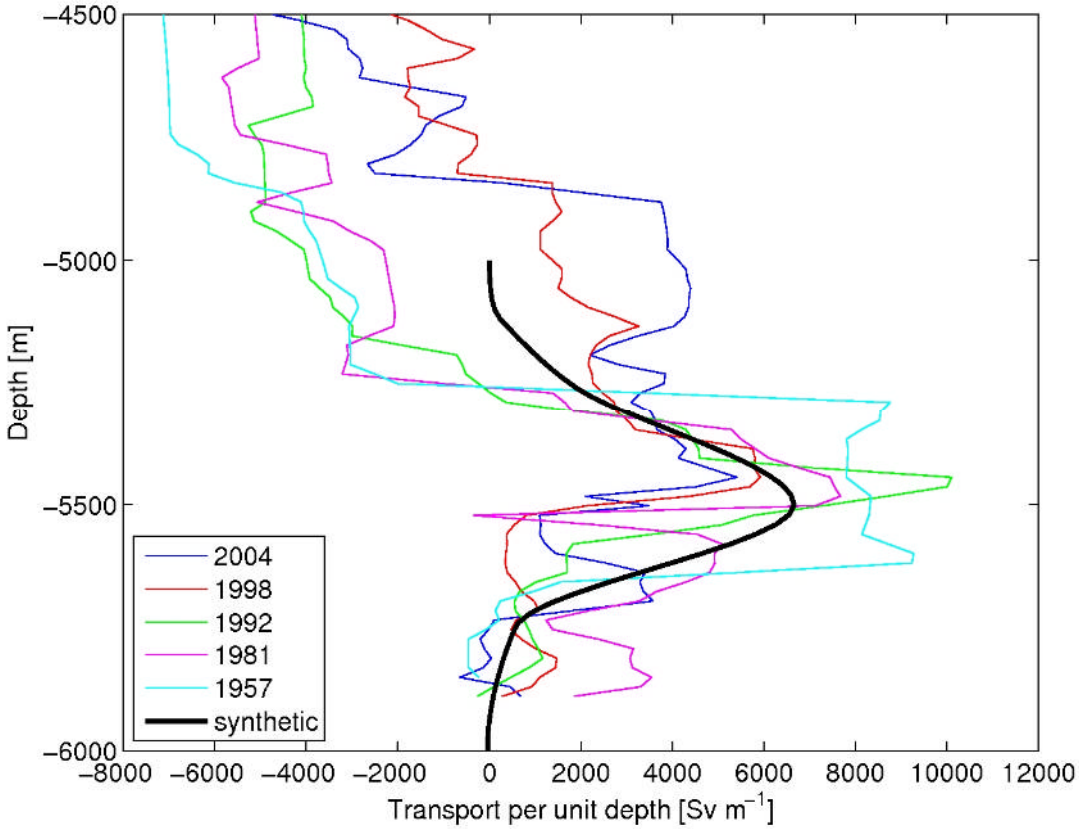

Fig. A1: Abyssal, zonally integrated transport across 26.5°N from hydrographic cruises in 1957, 1981, 1992, 1998, 2004 (as presented by Bryden et al., 2005). The synthetic approximation of the transports below 5000 m (black line) represents the transport shear profile used in this study to extend the AMOC transport profile $T_{AMOC}(z)$ into the AABW range.